Deep–Sea Research II 194 (2021) 104974

Contents lists available at ScienceDirect

Deep-Sea Research Part II

journal homepage: www.elsevier.com/locate/dsr2

Coupled modes of projected regional change in the Bering Sea from a dynamically downscaling model under CMIP6 forcing

Albert J. Hermann [a,b,*], Kelly Kearney [a,c], Wei Cheng [a,b], Darren Pilcher [a,b], Kerim Aydin [c], Kirstin K. Holsman [c], Anne B. Hollowed [c]

[a] Cooperative Institute for Climate, Ocean and Ecosystem Studies, University of Washington, Seattle, WA, 98195, USA
[b] Ocean Environment Research Division, NOAA/PMEL, Seattle, WA, 98195, USA
[c] Alaska Fisheries Science Center, NOAA, Seattle, WA, 98195, USA

ARTICLE INFO

Keywords:
Regional modeling
Bering sea
Climate change
Biophysical modeling
Integrated ecosystem assessment

ABSTRACT

Three different global earth system models from the Coupled Model Intercomparison Project Phase 6 (CMIP6) were used to explore anticipated changes in the Bering Sea under high (SSP126) and low (SSP585) carbon mitigation scenarios (i.e. low and high emission scenarios), via dynamical downscaling. A multivariate pattern analysis, based on Empirical Orthogonal Functions applied to monthly time series, reveals strong coupling of changes across several biophysical variables and the global forcing itself, on both yearly and multidecadal time scales. Rising air and ocean temperatures from the global models are strongly coupled with rising regional temperatures and reduced ice cover/thickness, as well as strong changes to the phenology of the plankton food chain, including reduced biomass of large zooplankton in the fall. This method ultimately provides a compact way to estimate the changes to many regional attributes under a variety of global change scenarios. Application of this method to a broad ensemble of the CMIP6 global model air temperatures suggests that compared to present conditions, the Bering Sea shelf bottom temperatures in July will warm by an average of ~4 degrees C by the end of the 21st century under SSP585, as compared with ~1 degrees C under SSP126, with greatest warming focused on the outer northern shelf.

1. Introduction

Widespread change is anticipated for the Bering Sea (AK) under climate change, including substantial oceanographic warming that scales with future carbon mitigation scenarios (IPCC 2013, 2014). Climate-driven changes to oceanographic conditions have the potential to propagate through the food web and impact fish and fisheries in the region (Holsman et al., 2018; Reum et al., 2020), with strong implications for most effective management of these resources (e.g. Holsman et al., 2020; Hollowed et al., 2020). The Bering Sea is a highly productive system that supports a wide diversity of species, some critically endangered, as well as multiple small coastal fishing communities that depend on subsistence harvest (Haynie and Huntington 2016) and large-scale commercial fisheries that annually represent more than 40% of the United States commercial landings (Fissel et al., 2017). In this paper, we report estimates of anticipated covarying changes to the physical and lower trophic level dynamics of the Bering Sea across space, time (by month), and variables, derived through the application of dynamical model downscaling to Coupled Model Intercomparison Project Phase 6 (CMIP6) global models, and subsequent Empirical Orthogonal Function (EOF)-based pattern analysis of the results. A direct description of downscaling results for individual model variables, as well as details of the global models used, can be found in a companion paper by Cheng et al. (2021, this volume; hereafter referred to as "C21").

1.1. Overview of the Bering Sea ecosystem

Prominent physical features of the Bering Sea include seasonal ice cover, strong advection of ice, and tidally generated biophysical domains. Ice formed each winter in the northern Bering Sea is advected to the southeast, where it gradually melts as it encounters warmer water and air temperatures. This southward advection contributes to the latitudinal salinity gradient of the Bering Sea and its interannual variability. A cross-shelf gradient in the vertical penetration of tidal mixing

* Corresponding author. Pacific Marine Environmental Laboratory, 7600 Sand Point Way NE, Seattle, WA, 98115, USA.
E-mail addresses: albert.j.hermann@noaa.gov (A.J. Hermann), kelly.kearney@noaa.gov (K. Kearney), wei.cheng@noaa.gov (W. Cheng), darren.pilcher@noaa.gov (D. Pilcher), kerim.aydin@noaa.gov (K. Aydin), kirstin.holsman@noaa.gov (K.K. Holsman), anne.hollowed@noaa.gov (A.B. Hollowed).

https://doi.org/10.1016/j.dsr2.2021.104974
Received 15 June 2021; Received in revised form 25 August 2021; Accepted 19 September 2021
Available online 7 October 2021

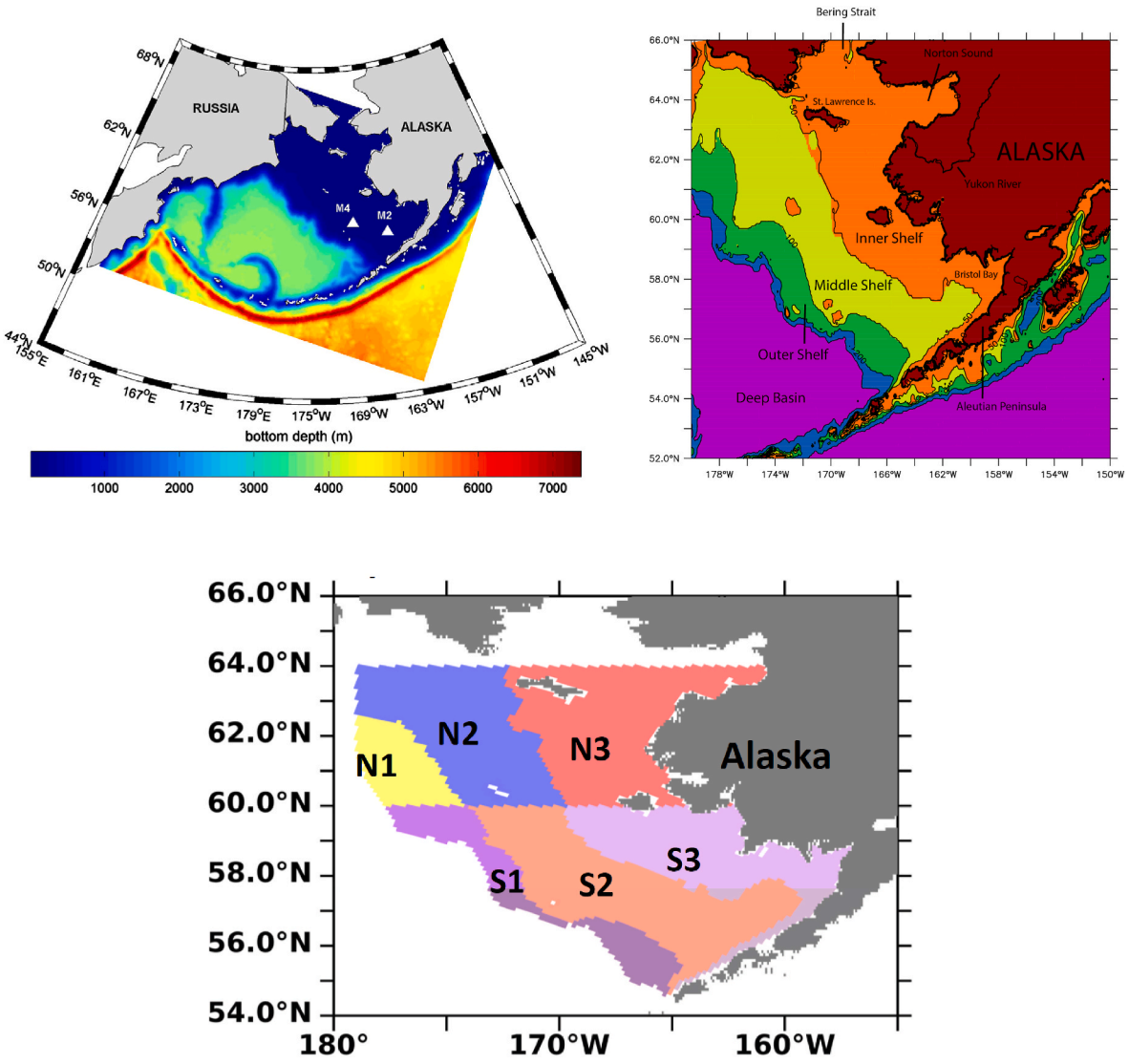

Fig. 1. Upper left panel: Domain and bathymetry of the regional model. Upper right panel: Bathymetry (m) with biophysical domains of the Bering Sea shelf. Orange = inner shelf domain (0–50m), yellow = middle shelf domain (50–100m), green = outer shelf domain (100–200m), blue = shelf break (200–1000m), purple = deep basin (>1000m). Lower center panel (from Cheng et al., 2021): Biophysical domains used to summarize spatial patterns; southern outer shelf (S1), southern middle shelf (S2), southern inner shelf (S3), northern outer shelf (N1), northern middle shelf (N2), and northern inner shelf (N3).

sets up distinct biophysical regimes with associated biota. Classically, the southeastern shelf is classified as having three biophysical domains: a vertically well-mixed inner shelf domain (ocean depth is between ~0 and 50m), a middle shelf domain (with ocean depth ~50–100m) which is well-mixed in the winter and has two distinct layers separated by a sharp thermocline in the summer, and an outer shelf domain (ocean depth ~100–200m) which is more gradually stratified (Kinder and Schumacher, 1981; Coachman, 1986; Kachel et al., 2002). A map of the region with these features identified is provided in Fig. 1.

Distinct biological features of the Bering Sea ecosystem include ice algae as a potential food source to secondary producers, and strong benthic-pelagic coupling. Within the different biophysical regimes, the relative magnitude of pelagic vs. benthic pathways of carbon flux varies interannually, and is believed to be strongly influenced by the extent of seasonal ice through its effects on stratification (Hunt et al., 2002, 2011). The relative importance of pelagic vs. benthic pathways is likely to shift under the influence of global warming, partially through its impact on seasonal ice extent in the Bering Sea. Field data suggest that cold temperatures in the Bering Sea lead to an increase in large crustacean zooplankton, favored as food items by juvenile pollock in the fall season (Coyle et al., 2011; Sigler et al., 2016).

The present hydrography and seasonal ice-driven climatology of the Bering Sea result in a highly productive ecosystem, with plankton biomass ultimately supporting large populations of shellfish and finfish (and major fisheries), marine birds and marine mammals (Sigler et al., 2016). Such intense production derives, in part, from a broad shelf with strong tidally-induced mixing, a plentiful supply of the micronutrient iron, and seasonal stratification, which maintains the phytoplankton in the euphotic zone, adjacent to a deep, macronutrient-rich basin. Interannual variation in winter ice extent over the Bering Sea modulates annual variability in productivity in system. A cold period in the Bering Sea from 2006 to 2011 (Stabeno et al., 2012) was followed by a return to warmer conditions, with reduced ice (Stabeno et al., 2016, 2017) and attendant changes in primary and secondary productivity (Sigler et al., 2016). Recent years have included marked reductions in ice cover (Stabeno and Bell, 2019) and the lowest Bering sea ice extent in 5500 years (Jones et al., 2020).

In previous studies, model-based multivariate analysis was used to help explore the relationships between physical and biological factors on the Bering Sea shelf (Hermann et al. 2013, 2019). These analyses

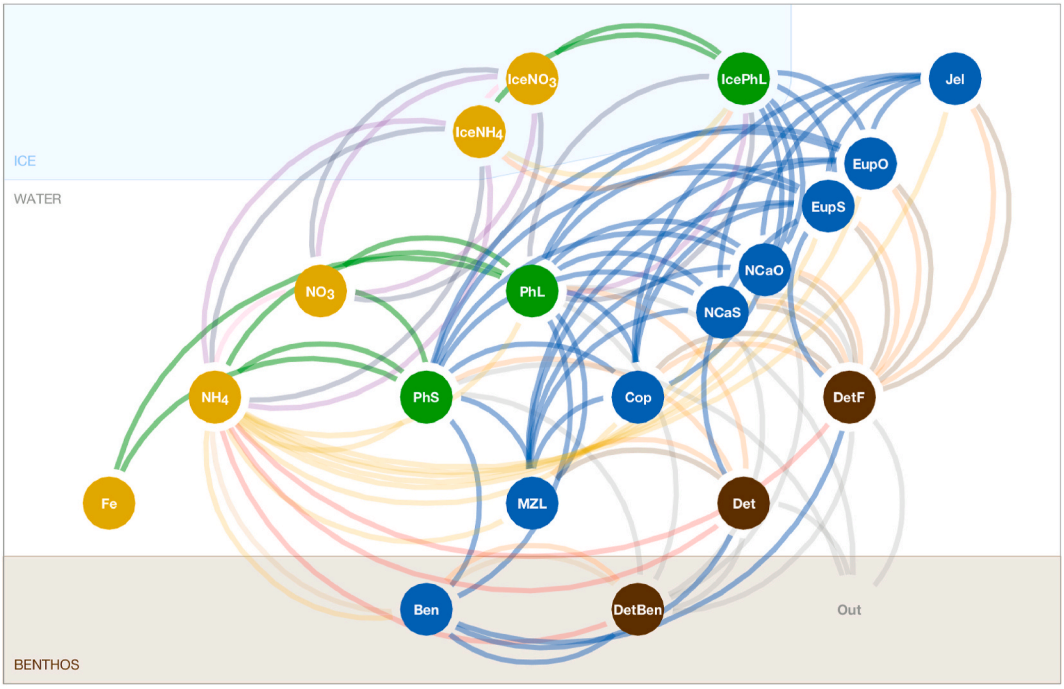

Fig. 2. Schematic of the BESTNPZ (from Kearney et al., 2020). State variable names are described in Table 1. Circular nodes represent state variables (gold indicates nutrient, green indicates producer, blue indicates consumer, brown indicates detritus). Edges (lines) represent fluxes between state variables and curve clockwise from source node to sink node. Edge colors indicate process type: green indicates primary production, blue indicates grazing and predation, brown indicates egestion, gold indicates respiration, red indicates remineralization, pink indicates nitrification, orange indicates non-predatory mortality, tan indicates excretion, purple indicates convective exchange, gray indicates sinking to seafloor, and navy indicates freezing/melting of ice.

suggested that the Bering Sea shelf may not respond uniformly to changes in climate forcing. For example, large crustacean zooplankton (*lcz*) were negatively correlated with temperature on the outer, southwestern shelf, but positively correlated to temperature on the inner, northeastern shelf. Areas of positive correlation tended to correspond with those areas with greatest change in ice cover. As in the revised Oscillating Control Hypothesis of Hunt et al. (2011), the ratio of large to total zooplankton was enhanced at lower temperatures. These results suggested that: 1) on the outer shelf, higher temperatures may be leading to reduced *lcz* production either through effects on stratification (and hence nutrient limitation), or through direct effects of temperature on growth, respiration, predation and vertical migration; 2) changes on the northern shelf may involve a complex interplay of light and nutrient limitation effects, as modulated by a reduction in the duration of seasonal ice cover.

Ice dynamics of the Bering Sea have been explored in both observational and modeling studies (Stabeno et al., 2010; Danielson et al., 2011; Cheng et al., 2014; Li et al., 2014a, b; Sullivan et al., 2014, Jones et al., 2020). Ice is formed seasonally in the northern Bering Sea and is advected southward, resulting in a net transfer of fresh water from north to south. Heat budgets from these studies have underscored the importance of sensible heat flux between the atmosphere and the ice in the northern Bering, and between the ocean surface and the ice in the southern Bering, where the ice edge retreats each spring.

1.2. Contrast with previous downscaling studies

In previous publications (Hermann 2013, 2016a), we projected future Bering Sea conditions to 2040 under an intermediate carbon mitigation scenario (i.e., A1B) from phase 3 of the Coupled Model Intercomparison (CMIP3; Meehl et al., 2007). In a more recent study (Hermann et al., 2019, henceforth referred to as "H19") these were extended to 2100 and included a larger ensemble of global models under low mitigation (i.e. high emission, RCP 8.5) and moderate mitigation (i.e. moderate emission, RCP 4.5) scenarios from phase 5 of the CMIP (CMIP5; Taylor et al., 2012). Here, we focus on the latest set of global results (CMIP6) out to 2100 under two different Shared Socioeconomic Pathways (SSPs), specifically the low mitigation (high emission, SSP585) and high mitigation (low emission, SSP126) scenarios (O'Neill et al., 2016) using an extension of the multivariate methods described in H19. As described in C21, the CMIP5 and CMIP6 results differ in their equilibrium climate sensitivity (ECS), that is, their temperature response to increased greenhouse gases. Further, whereas the focus of H19 was on annually averaged change over the entire Bering Sea shelf and basin, here our focus is refined specifically to the Bering Sea shelf and the individual months of each year. The multivariate approach, now applied to monthly rather than yearly anomalies, helps to elucidate changes that are coupled across different variables, including changes to the phenology of each variable within the larger biophysical system. As with the CMIP5-based results, these multivariate methods are used to statistically expand our 6-member dynamically downscaled ensemble to include all available CMIP6 global projections in a dynamically consistent manner. The revised, monthly-based method used now allows for any shifts in the phenology of the forcing itself to influence the monthly regional results. Output from these simulations will be used in fisheries models, both to project stocks and for management-strategy evaluation, as part of NOAA's Alaska Climate Integrated Modeling Project (ACLIM; Hollowed et al., 2020).

2. Methods

2.1. The global earth system models

Output from three different global Earth System Models (ESMs) were used in this study: 1) CESM version 2 with Community Atmospheric Model version 6 (CESM2-CAM6; Danabasoglu et al., 2020); 2) GFDL Earth System Model version 4.1 (GFDL-ESM4; Dunne et al., 2020); 3) MIROC-Earth System version 2 for Long-term simulations

Table 1
State variables of the regional biological model.

Variable	Description	Units
NO3	nitrate	mmol N m^{-3}
NH4	ammonium	mmol N m^{-3}
PhS	small phytoplankton (cells less than 10 μm diameter)	mg C m^{-3}
PhL	large phytoplankton (bloom-forming diatoms)	mg C m^{-3}
MZL	microzooplankton	mg C m^{-3}
Cop	small-bodied copepods (e.g., Pseudocalanus spp.)	mg C m^{-3}
NCaS	on-shelf large-bodied copepods (primarily *Calanus marshallae*)	mg C m^{-3}
EupS	on-shelf euphausiids (primarily Thysanoessa raschii)	mg C m^{-3}
NCaO	off-shelf large-bodied copepods (primarily Neocalanus spp.)	mg C m^{-3}
EupO	off-shelf euphausiids (primarily Thysanoessa inermis)	mg C m^{-3}
Det	slow-sinking detritus	mg C m^{-3}
DetF	fast-sinking detritus	mg C m^{-3}
Jel	jellyfish (Chrysaora melanaster)	mg C m^{-3}
Fe	iron	μmol Fe m^{-3}
Ben	benthic infauna (bivalves, amphipods, polychaetes, etc.)	mg C m^{-2}
DetBen	benthic detritus	mg C m^{-2}
IcePhL	ice algae	mg C m^{-3}
IceNO3	ice nitrate	mmol N m^{-3}
IceNH4	ice ammonium	mmol N m^{-3}

(MIROC-ES2L; Hajima et al., 2020). These are hereafter referred to as "CESM", "GFDL", and "MIROC", respectively. We focused on high (SSP126) and low (SSP585) carbon mitigation scenarios ("Shared Socioeconomic Pathways"; O'Neill et al., 2016), and used output from both the "historical" period (specifically, 1980–2014) and future projections (2015–2100). As in H19, these models were chosen to span a range of possible futures by including a broad range of model structures and possible emission scenarios. A detailed description of these different models, and the rationale for their use in our study, is provided in the C21 companion manuscript.

2.2. The regional downscaling model

Major features of the regional model ("Bering10K") are as follows. The model is based on the Regional Ocean Modeling System (ROMS) version 3.2. ROMS is a terrain-following model with curvilinear horizontal coordinates; a description of basic features and implementation can be found in Haidvogel et al. (2008) and Shchepetkin and McWilliams (2005). The Bering10K regional grid has approximately 10 km horizontal resolution, with 30 vertical levels (hereafter, K20), a significant enhancement from the 10-layer version used in H19 (Kearney et al., 2020). This finer resolution better captures the evolution of stratification on the shelf, and the seasonal destruction of the summer mixed layer in particular. Fine-scale bathymetry is based on soundings from NOS, NOAA, and other sources as described in Danielson et al. (2011); smoothing of that bathymetry was utilized for numerical stability. Any oceanic regions shallower than 10 m were set to be 10 m deep. Mixing is based on the algorithms of Large et al. (1994). Both ice (Budgell, 2005) and tidal dynamics are included in this model; the explicit inclusion of tidal flows allows tidally generated mixing and tidal residual flows to develop. Freshwater runoff was applied by freshening of the surface salinity field within a few grid points of the coastline, based on climatological monthly runoff values developed by Kearney (2019). Bulk forcing, based on algorithms of Large and Yeager (2008), were used to relate winds, air temperature, relative humidity, and downward shortwave and longwave radiation to surface stress and the net transfers of sensible heat, latent heat, net shortwave and net longwave radiation through the sea surface. Further details of model tuning, implementation and biases are available in Hermann et al. (2016a) and Kearney et al. (2020).

Table 2
Properties used in the multivariate analysis. Variables in plain text are from the regional model, those in **bold** are boundary conditions from the global models, and those in ***bold italic*** are surface forcing from the global models.

Jel_integrated	Jellyfish concentration, integrated over depth	mg C m^{-2}
NCaS_surface5m	On-shelf large copepod concentration, surface 5m mean	mg C m^{-3}
NCaO_surface5m	Offshore large copepod concentration, surface 5m mean	mg C m^{-3}
EupS_integrated	On-shelf euphausiid concentration, integrated over depth	mg C m^{-2}
EupO_integrated	Offshore euphausiid concentration, integrated over depth	mg C m^{-2}
Cop_surface5m	Small copepod concentration, surface 5m mean	mg C m^{-3}
MZL_surface5m	Microzooplankton concentration, surface 5m mean	mg C m^{-3}
PhL_surface5m	Large phytoplankton concentration, surface 5m mean	mg C m^{-3}
PhS_surface5m	Small phytoplankton concentration, surface 5m mean	mg C m^{-3}
Iron_bottom5m	iron concentration, bottom 5m mean	micromol Fe m^{-3}
Iron_surface5m	iron concentration, surface 5m mean	micromol Fe m^{-3}
NH4_bottom5m	Ammonium concentration, bottom 5m mean	mmol N m^{-3}
NH4_surface5m	Ammonium concentration, surface 5m mean	mmol N m^{-3}
NO3_bottom5m	Nitrate concentration, bottom 5m mean	mmol N m^{-3}
NO3_surface5m	Nitrate concentration, surface 5m mean	mmol N m^{-3}
v_1	Along-shelf velocity, bottom layer	m s^{-1}
u_1	Cross-shelf velocity, bottom layer	m s^{-1}
v_30	Along-shelf velocity, top layer	m s^{-1}
u_30	Cross-shelf velocity, top layer	m s^{-1}
hice_30	average ice thickness in cell	m
aice_30	fraction of cell covered by ice	(no units)
salt_surface5m	salinity, surface 5m mean	psu
temp_bottom5m	potential temperature, bottom 5m mean	Celsius
temp_surface5m	potential temperature, surface 5m mean	Celsius
v_south	Along-shelf velocity at southeastern boundary, top layer	m s^{-1}
u_south	Cross-shelf velocity at southeastern boundary, top layer	m s^{-1}
temp_south	potential temperature at southeastern boundary, top layer	Celsius
salt_south	Salinity at southeastern boundary, top layer	psu
no3_south	Nitrate at southeastern boundary, top layer	mmol N m^{-3}
nh4_south	Ammonium at southeastern boundary, top layer	mmol N m^{-3}
iron_south	iron at southeastern boundary, top layer	micromol Fe m^{-3}
v_west	Along-shelf velocity at southwestern boundary, top layer	m s^{-1}
u_west	Cross-shelf velocity at southwestern boundary, top layer	m s^{-1}
temp_west	potential temperature at southwestern boundary, top layer	Celsius
salt_west	Salinity at southwestern boundary, top layer	psu
no3_west	Nitrate at southwestern boundary, top layer	mmol N m^{-3}
nh4_west	Ammonium at southwestern boundary, top layer	mmol N m^{-3}
iron_west	iron at southwestern boundary, top layer	micromol Fe m^{-3}
Vwind_frc	Northward wind from global model	m s^{-1}
Uwind_frc	Eastward wind from global model	m s^{-1}
Tair_frc	Air temperature from global model	Celsius
swrad_frc	Shortwave radiation from global model	Watts m^{-2}
rain_frc	Rainfall from global model	m s^{-2}
Qair_frc	Absolute humidity from global model	g g^{-1}
Pair_frc	Surface air pressure from global model	Pa
lwrad_down_frc	Downwelling longwave radiation from global model	Watts m^{-2}

The lower trophic level dynamics (Nutrient-Phytoplankton-Zooplankton; NPZ) model was initially developed by Gibson and Spitz (2011) and was used in H19. The most recent version of this NPZ model

(K20), used in the present study, was extensively documented, validated and examined for biases in Kearney et al. (2020), and is displayed in Fig. 2. Briefly, this model includes two size categories of phytoplankton (*PhS, PhL*) and ice plankton (*IcePhL*), and distinguishes among microzooplankton (*MZL*), small copepods (*Cop*), large copepods (*NCaS, NCaO*) and euphausiids (*EupS, EupO*), as well as jellyfish (*Jel*), benthic detritus (*DetBen*), and benthic infauna (*Ben*). Limiting nutrients are nitrate (*NO3*), ammonium (*NH4*) and dissolved iron (*Fe*). Metabolic and grazing rates are temperature dependent, which leads to substantially different food web structure under cold vs. warm conditions. A full list of biological components is shown in Table 1; note that "onshore" and "offshore" categories of large zooplankton refer to slightly different species groupings with associated diet preferences and diapause behavior. Results from hindcasts and forecasts with an earlier version of this model are described in Hermann et al. (2013, 2016a) and Ortiz et al. (2016); projections using that previous version are described in H19. Hindcasts with the most recent version are compared with observations in Kearney et al. (2020). In addition to higher vertical resolution (30 layers) this most recent version includes: 1) improved formulation for the role of chlorophyll, sediment, and organic matter on the attenuation of light as used for phytoplankton photosynthesis and water column distribution of surface heat fluxes, 2) correction of non-mass-conservative behavior within the biological module, 3) removal of macronutrient nudging except at the lateral boundaries, and 4) adjustment of the euphausiid prey preferences to allow for detrital scavenging in winter. Kearney et al. (2020) includes a detailed description of the two versions. In both versions, light attenuation by sediment was a time-invariant function of local bathymetry (higher attenuation in shallow areas); in the present version, this function was explicitly calibrated using satellite (VIIRS) optical data. Most recently, carbonate dynamics have been added to this model (Pilcher et al., 2021, this volume). While the inclusion of carbonate variables was beyond the scope of our statistical analysis, many of the state variables from Table 1 were utilized, sampled at specific layers or averaged over specific depths (Table 2).

Atmospheric forcing of the regional model is derived from linear interpolation of daily global ESM results, for application to the bulk formulae of the regional model. Lateral open boundary conditions used the radiation plus nudging scheme of Marchesiello et al. (2001) for both physical and biological scalars, as well as baroclinic velocities. Interannually varying monthly velocities, temperature, salinity, sea surface height, nitrate, ammonium, and dissolved iron values were interpolated from the ESMs to all depths of the Bering10K boundaries; for the plankton state variables, zero values were used (internally, under inflow conditions, the model quickly spins up plankton from the provided nutrients within a short distance from the boundary). For monthly coastal runoff, we modulated the monthly climatologies of Kearney et al. (2019) using the ratio of projected to present spatially averaged annual runoff (the latter being derived from the "historical" period of each global model), where the spatial average is taken over the Bering Sea plus Alaska (115-217°E and 44-71°N). Hence, for any future year, the calculated yearly runoff is a function of the projected yearly regional runoff from the ESM, but the presently observed phenology and spatial distribution of the runoff is retained from our regional model hindcasts (Kearney et al., 2020).

Further details on the Bering10K model structure used here, as well as an extensive comparison of hindcast results with an extensive set of physical observations and biological observations, can be found in Kearney et al. (2020). The hindcast is driven by relatively coarse (>50 km) large-scale atmospheric and oceanic reanalyses. Despite that relatively coarse forcing, the hindcast demonstrates considerable skill in capturing the observed seasonal climatology and interannual variability in patterns of ice cover and bottom temperature, the seasonal climatology of circulation, mixing, and stratification, and the mean seasonal cycle of primary production on the southeastern Bering Sea Shelf. Based on the available biological data, more limited skill was observed for domain-wide patterns of nutrient cycling, primary production and zooplankton community structure. Additional comparisons of hindcast results with available biophysical data for earlier versions of Bering10K are described in Hermann et al. (2013, 2016a, 2019).

A comparison of downscaling results driven by forcing from the "historical" period of each ESM (1980–2014) with climatological observations of sea-ice cover and bottom temperature is described in C21. In particular, this comparison demonstrates how each of the historical downscaling runs captures the observed pattern of mean sea-ice concentrations in March (the month with the most extensive ice cover), and the observed pattern of bottom temperatures in July. Collectively these direct hindcast and ESM-based historical comparisons indicate that, despite remaining known and possible unknown biases (due to limited observations), the Bering10K model provides a useful framework to explore potential changes to the region driven by climate change.

2.3. The statistical method

In a previous publication centered on the downscaling of CMIP5 projections (H19), we utilized a multivariate EOF analysis to ascertain coupled changes to annually averaged patterns of multiple variables over the entire Bering Sea shelf and basin. Here, for the CMIP6-based results, we restrict our spatial focus to the Bering Sea shelf (areas shallower than 200m, from the Aleutian Islands in the south to the Bering Strait in the north), but expand our focus to include each month of each year, using monthly averaged perturbations from the monthly climatologies of each downscaling model run.

This multivariate analysis of CMIP6-based results is in many ways complementary to the univariate analyses of C21. While that work is focused on projected long-term changes of individual variables, the present work seeks to find any sets of interannual changes (including those spanning the earlier and later parts of the 21st century) which covary across variables and time-of-year; hence its emphasis is emergent behaviors of the entire biophysical system. As in H19, this approach has the added benefit of providing a compact statistical model of the downscaling model's behavior, which can ultimately be used for compact downscaling of other global ESM results. The most significant differences with the methods of H19 are: 1) a focus on the Bering Sea shelf, rather than the entire basin; 2) a focus on individual months, rather than yearly averages.

Our approach is related to what is sometimes termed "extended" or "combined" EOF analysis, and shares some features with the methods described by Thorson et al. (2020), as well as earlier studies of the Bering Sea and the Gulf of Alaska (Hermann et al. 2013, 2016b). Reviews of EOF-related methods can be found in Bretherton et al. (1992) and Preisendorfer (1988). Our method is perhaps most closely related to what is termed Canonical Correlation Analysis (CCA), but whereas CCA is typically applied to explore connections between two variable fields, here it is applied to a much larger set of variables. It is important to emphasize that EOF analysis deals with independent realizations of a collection of variables. In typical oceanographic usage of EOFs, these consist of time series of measured values of a single variable at multiple locations - each "realization" consists of the value at the same time at each of many locations. By contrast, in typical biological oceanographic usage of Principal Component (PC) analysis, each realization consists of a measurement of multiple variables at a particular location and time. In the present circumstance, we will use measurements of multiple variables at a grid of locations on each month of the same calendar year. Our statistical technique then seeks out dominant patterns of correlation relating particular variables and months - for example nutrients in month p correlating with plankton in month q. For this analysis, each calendar year constitutes a single realization of that collection of measurements.

The particular variables chosen for use in our statistical analysis include major physical and biological attributes of the system (Table 2); these are necessarily a subset of all possible variables from the forcing

Table 3
List of global model datasets for air temperature (Tair) used in statistical downscaling under SSP126 (see https://wcrp-cmip.github.io/CMIP6_CVs/docs/CMIP6_source_id.html for model details regarding each model/realization).

SSP126
ACCESS-CM2_ssp126_r1i1p1f1_gn
ACCESS-CM2_ssp126_r2i1p1f1_gn
ACCESS-ESM1-5_ssp126_r1i1p1f1_gn
ACCESS-ESM1-5_ssp126_r2i1p1f1_gn
AWI-CM-1-1-MR_ssp126_r1i1p1f1_gn
BCC-CSM2-MR_ssp126_r1i1p1f1_gn
CAMS-CSM1-0_ssp126_r1i1p1f1_gn
CAMS-CSM1-0_ssp126_r2i1p1f1_gn
CanESM5_ssp126_r1i1p1f1_gn
CanESM5_ssp126_r2i1p1f1_gn
CAS-ESM2-0_ssp126_r1i1p1f1_gn
CESM2-WACCM_ssp126_r1i1p1f1_gn
CIESM_ssp126_r1i1p1f1_gr
CMCC-CM2-SR5_ssp126_r1i1p1f1_gn
CMCC-ESM2_ssp126_r1i1p1f1_gn
CNRM-CM6-1-HR_ssp126_r1i1p1f2_gr
CNRM-CM6-1_ssp126_r1i1p1f2_gr
CNRM-ESM2-1_ssp126_r1i1p1f2_gr
EC-Earth3_ssp126_r1i1p1f1_gr
EC-Earth3-Veg-LR_ssp126_r1i1p1f1_gr
EC-Earth3-Veg-LR_ssp126_r2i1p1f1_gr
EC-Earth3-Veg_ssp126_r1i1p1f1_gr
EC-Earth3-Veg_ssp126_r2i1p1f1_gr
FGOALS-f3-L_ssp126_r1i1p1f1_gr
FGOALS-g3_ssp126_r1i1p1f1_gn
FGOALS-g3_ssp126_r2i1p1f1_gn
GFDL-ESM4_ssp126_r1i1p1f1_gr1
GISS-E2-1-G_ssp126_r1i1p1f2_gn
IITM-ESM_ssp126_r1i1p1f1_gn
KIOST-ESM_ssp126_r1i1p1f1_gr1
MCM-UA-1-0_ssp126_r1i1p1f2_gn
MIROC-ES2L_ssp126_r1i1p1f2_gn
MPI-ESM1-2-HR_ssp126_r1i1p1f1_gn
MPI-ESM1-2-HR_ssp126_r2i1p1f1_gn
MRI-ESM2-0_ssp126_r1i1p1f1_gn
NESM3_ssp126_r1i1p1f1_gn
NESM3_ssp126_r2i1p1f1_gn
NorESM2-LM_ssp126_r1i1p1f1_gn
NorESM2-MM_ssp126_r1i1p1f1_gn
TaiESM1_ssp126_r1i1p1f1_gn
UKESM1-0-LL_ssp126_r1i1p1f2_gn

Table 4
List of global model datasets for air temperature (Tair) used in statistical downscaling under SSP585 (see https://wcrp-cmip.github.io/CMIP6_CVs/docs/CMIP6_source_id.html for model details regarding each model/realization).

SSP585
ACCESS-CM2_ssp585_r1i1p1f1_gn
ACCESS-CM2_ssp585_r2i1p1f1_gn
ACCESS-ESM1-5_ssp585_r1i1p1f1_gn
ACCESS-ESM1-5_ssp585_r2i1p1f1_gn
AWI-CM-1-1-MR_ssp585_r1i1p1f1_gn
BCC-CSM2-MR_ssp585_r1i1p1f1_gn
CAMS-CSM1-0_ssp585_r1i1p1f1_gn
CAMS-CSM1-0_ssp585_r2i1p1f1_gn
CanESM5_ssp585_r1i1p1f1_gn
CanESM5_ssp585_r2i1p1f1_gn
CAS-ESM2-0_ssp585_r1i1p1f1_gn
CESM2-WACCM_ssp585_r1i1p1f1_gn
CESM2-WACCM_ssp585_r2i1p1f1_gn
CIESM_ssp585_r1i1p1f1_gr
CMCC-CM2-SR5_ssp585_r1i1p1f1_gn
CMCC-ESM2_ssp585_r1i1p1f1_gn
CNRM-CM6-1-HR_ssp585_r1i1p1f2_gr
CNRM-CM6-1_ssp585_r1i1p1f2_gr
CNRM-ESM2-1_ssp585_r1i1p1f2_gr
EC-Earth3_ssp585_r1i1p1f1_gr
EC-Earth3-Veg-LR_ssp585_r1i1p1f1_gr
EC-Earth3-Veg-LR_ssp585_r2i1p1f1_gr
EC-Earth3-Veg_ssp585_r1i1p1f1_gr
EC-Earth3-Veg_ssp585_r2i1p1f1_gr
FGOALS-f3-L_ssp585_r1i1p1f1_gr
FGOALS-g3_ssp585_r1i1p1f1_gn
FGOALS-g3_ssp585_r2i1p1f1_gn
GFDL-ESM4_ssp585_r1i1p1f1_gr1
GISS-E2-1-G_ssp585_r1i1p1f2_gn
IITM-ESM_ssp585_r1i1p1f1_gn
KIOST-ESM_ssp585_r1i1p1f1_gr1
MCM-UA-1-0_ssp585_r1i1p1f2_gn
MIROC-ES2L_ssp585_r1i1p1f2_gn
MPI-ESM1-2-HR_ssp585_r1i1p1f1_gn
MPI-ESM1-2-HR_ssp585_r2i1p1f1_gn
MRI-ESM2-0_ssp585_r1i1p1f1_gn
NESM3_ssp585_r1i1p1f1_gn
NESM3_ssp585_r2i1p1f1_gn
NorESM2-LM_ssp585_r1i1p1f1_gn
NorESM2-MM_ssp585_r1i1p1f1_gn
TaiESM1_ssp585_r1i1p1f1_gn
UKESM1-0-LL_ssp585_r1i1p1f2_gn

and regional models. They are chosen to emphasize mean quantities near the ocean surface, where much of the primary production takes place, at the ocean bottom, of particular interest to fisheries in the Bering Sea, and in the case of larger zooplankton and jellyfish, integrated through the water column. They also include atmospheric forcing from the global models, as well as ocean surface quantities from the global models at the southeast and southwest boundaries of the regional model, where the ESMs provide the boundary conditions. Benthic categories and carbonate variables were not included in the set; however, these will be explored in future studies. The surface and bottom ocean velocities used in this set are defined in the "native" coordinates of the ROMS grid, which is roughly oriented in "cross-shelf" and "along-shelf" directions.

For the EOF analysis we utilize all six dynamically downscaling runs of the Bering10K model, spanning three different global model types (CESM, GFDL, and MIROC) and two different Shared Socioeconomic Pathways (SSP126 and SSP585) over years 85 years (2015–2099). These models are described in the companion paper C21. We first calculate the monthly average deviations from monthly climatology within each run separately; this results in six sets of perturbation time series for each of the ROMS grid points, ordered in time. These are binned into 50-km squares using the native ROMS grid. We then take all six sets of deviation time series and concatenate them together into one long $85 \times 6 = 510$ member set. In effect, each year of each model is considered to provide us with an independent sample of the multivariate collection for each of the twelve months of the year. These samples are used for the covariance analysis across variables and months - that is, the method seeks out what aspects of the system, including phenology, tend to occur together in any given year.

As in H19, to expedite the multivariate analysis, we dimensionally reduce the spatial and temporal patterns of each single variable and month with univariate EOFs. The collection of time series (PCs) from this univariate analysis is then used to investigate covariance across variables and months, which can subsequently be used in prediction. The overall procedure can be summarized as:

1) Using monthly anomaly time series from the dynamical downscaling (both the ESM forcing and the regional response), separately derive univariate EOFs for each variable and each month of the year. This yields a set of spatial loading patterns and modulating yearly time series for each variable/month combination.
2) Scale each of the yearly time series according to the variance explained by the corresponding EOF. For each variable/month, retain only those time series corresponding to the ten leading EOF patterns (univariate_modes) for that particular variable/month.
3) Apply Principal Component analysis to that scaled, reduced set of yearly time series. This yields a set of loadings for each variable/month/univariate_mode, and a "master" set of yearly time series

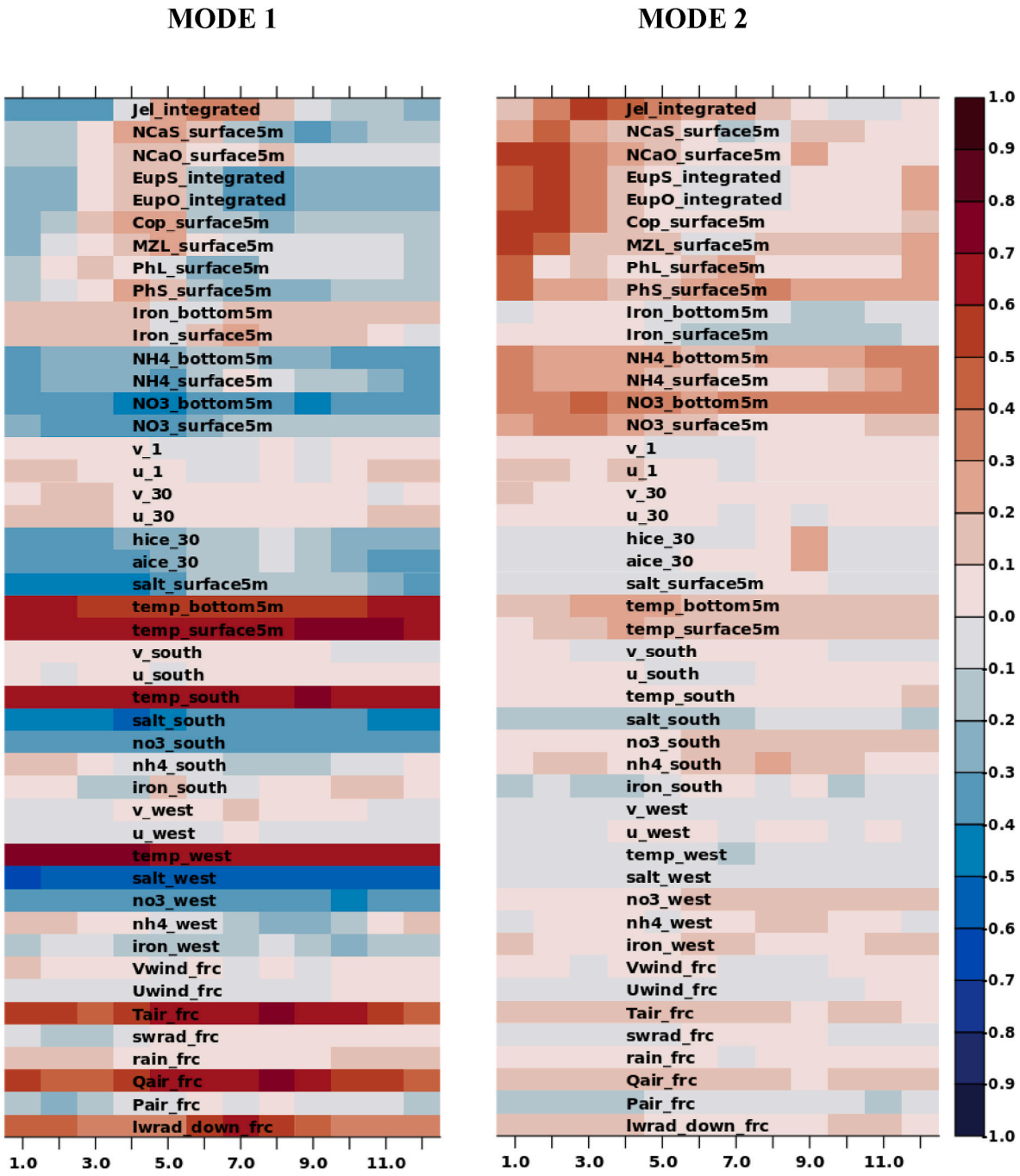

Fig. 3. Leading two multivariate modes **M** of within-year covariability among the topmost univariate EOFs of selected biophysical variables (ordinate) for each month of the year (abcissa). A positive/negative sign denotes the positive/negative correlation among spatial patterns; each spatial pattern has a positive spatial mean. See Table 2 for variable descriptions.

(Principal Components with annual values) which modulate those multivariate loadings through time.

4) For each variable/month, derive the spatial patterns (multivariate spatial modes) corresponding to that "master" set of yearly time series.
5) Project additional sets of ESM forcing onto the multivariate spatial modes corresponding to that forcing variable and month, in order to predict the monthly anomalies that would have been obtained if such forcing had been dynamically applied to the regional model.

We now present a more detailed motivation and description of the procedure. A priori we know that the mean spatial patterns of a single variable are substantially different in each month (for example, the seasonal evolution and destruction of the "cold pool" in the Bering Sea), and we could attempt to remove this "primary" known signal by looking at a continuous series of deviations from the monthly climatology. This is in fact commonly done in univariate EOF of the ocean; the underlying assumption is that the deviations are normally distributed about the monthly climatology. However, for biological variables especially (and for some physical variables as well), the monthly climatology includes strong shifts in space from one month to the next (for example, a phytoplankton bloom which migrates across the shelf, or the seasonal progression of the Bering Sea cold pool). As a result, the spatial patterns of deviations from monthly climatology will *themselves* vary month by

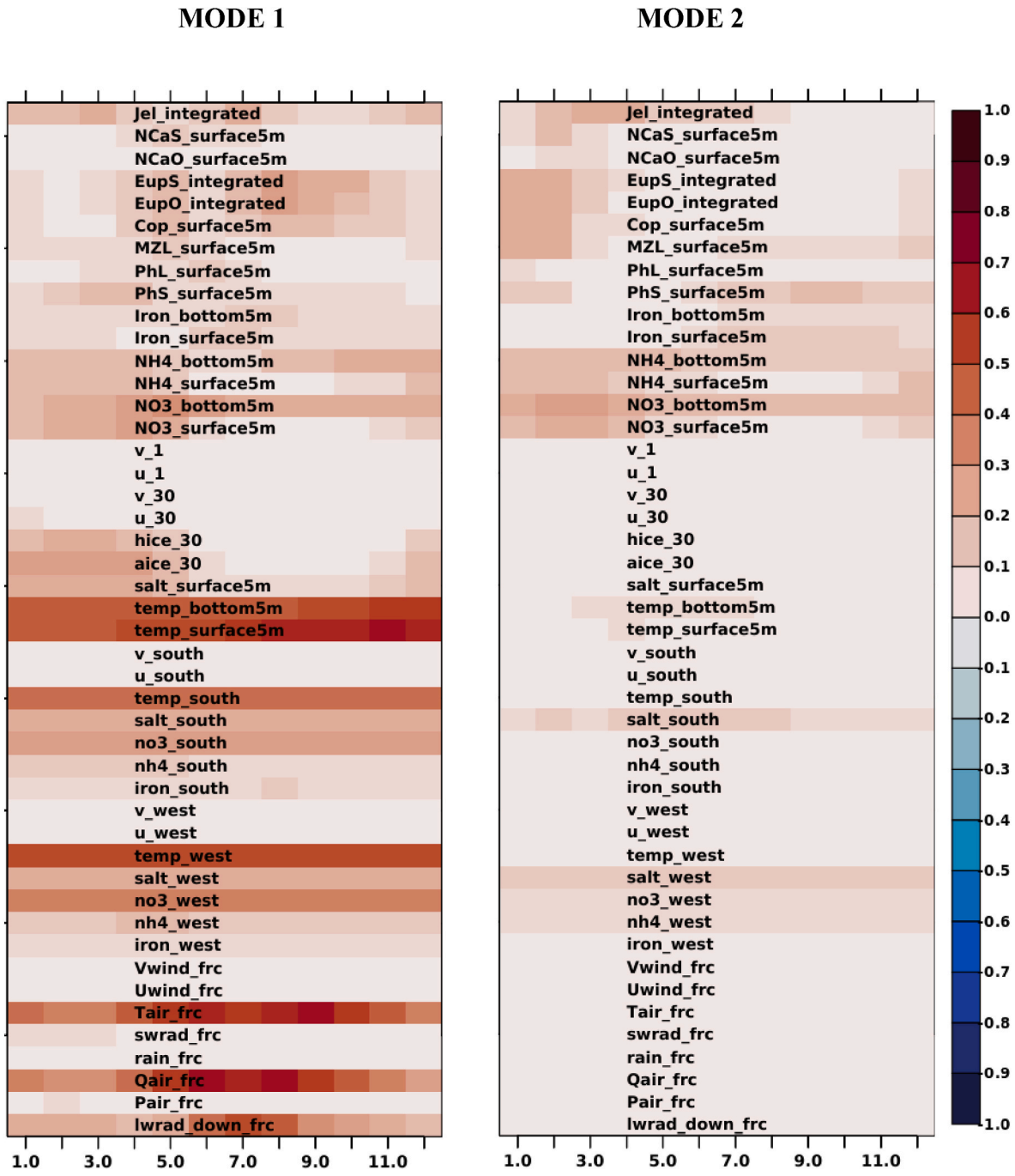

Fig. 4. As in Fig. 3, here illustrating the areal-averaged fractional variance of the original dataset explained by each of the two leading multivariate modes.

month in a systematic fashion, and this complex spatial migration would be difficult to capture with a few spatial modes if we used continuous time series of month-by-month perturbations. A more effective way to capture the interannual variability of the system is to treat each month and variable as a separate multiyear time series. A matrix notation for this EOF decomposition is as follows:

$$\mathbf{U_{kl}}^{\mathbf{ij}} = \mathbf{X_{kn}}^{\mathbf{ij}} * \mathbf{T_{nl}}^{\mathbf{ij}} \quad (1)$$

where we have used subscripts to indicate the row and column dimensions of each matrix, and superscripts to identify the variable-month being decomposed. The asterisk symbol (*) here denotes matrix multiplication. Hence $\mathbf{U_{kl}}^{\mathbf{ij}}$ represents the concatenated multiyear time series of variable i (e.g. surface temperature) during month j (e.g. May) at location k (a specific latitude, longitude, depth) during each year of each ESM/SSP combination l (e.g. calendar year 2050 from the downscaling run based on GFDL SSP585). To summarize:

i = 1,...number of variables (I)
j = 1,...number of months (J=12)
k = 1…number of locations (K)
l = 1...number of ESM/SSP/yearly samples (L = 510)
n = 1...number of independent EOF modes (N = min (K,L))

For each ij, $\mathbf{X_{kn}}^{\mathbf{ij}}$ is the mode n spatial pattern (with units of the original variable) capturing the covariability among different spatial locations k for variable i during month j, and $\mathbf{T_{nl}}^{\mathbf{ij}}$ are the set of *unit-variance, zero-mean* time series modulating each of those spatial modes, each with one value per yearly sample. In this manner the original time

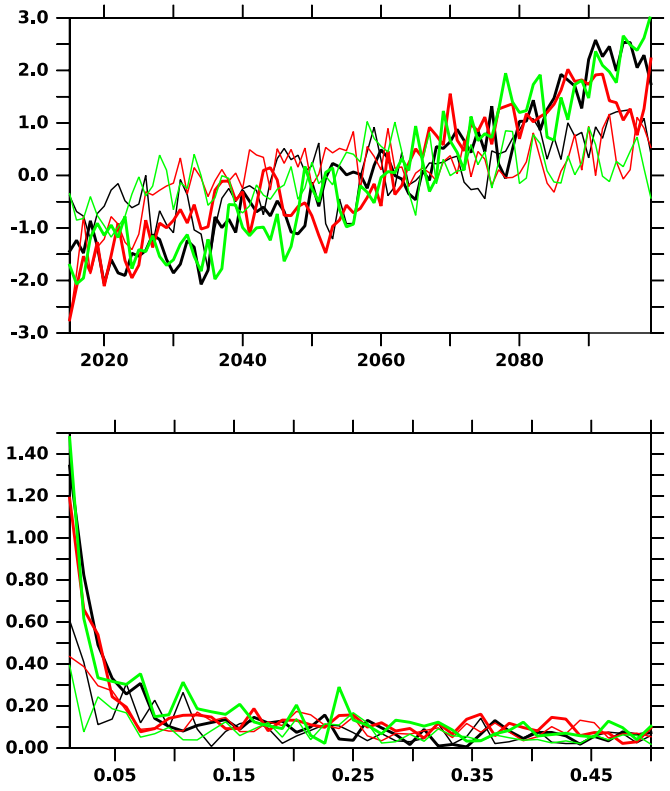

Fig. 5. Upper panel: Yearly time series modulating the Mode 1 monthly spatial patterns of covarying change for each of the global models and socioeconomic pathways. Black = CESM, Red = GFDL, Green = MIROC; thin lines are SSP126, thick lines are SSP585. The ordinate shows the (unitless) amplitude of the modulating time series; the abscissa shows the calendar year (one value per year for each model realization). Lower panel: Power spectra of each time series, showing variance (ordinate) as a function of cycles per year (abscissa).

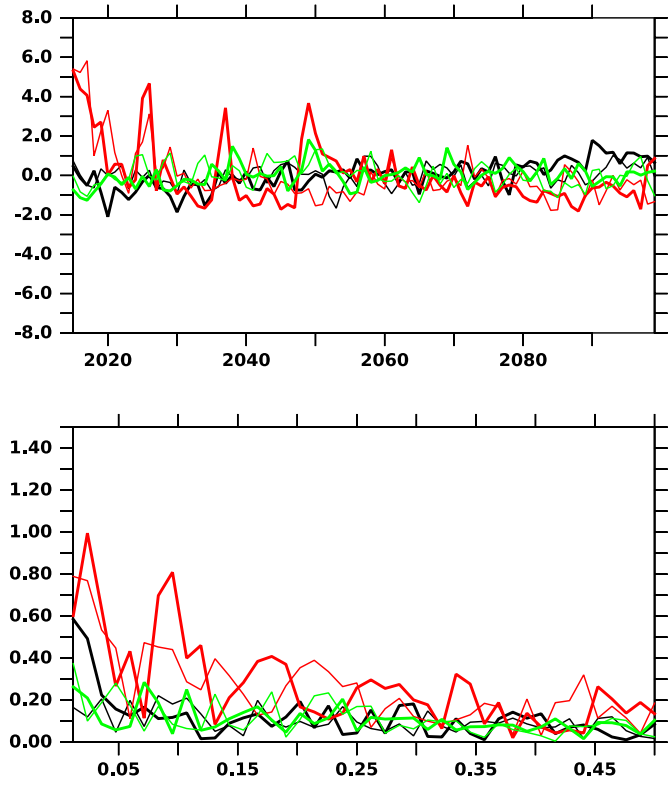

Fig. 6. As in Fig. 5, for Mode 2.

series **U** are efficiently described using a limited number of modes **X** with amplitudes **T** specific to each yearly sample.

Note that each $\mathbf{U}^{ij}$ has *K* rows and *L* columns, each $\mathbf{X}^{ij}$ has *K* rows and *N* columns, and each $\mathbf{T}^{ij}$ has *N* rows and *L* (in our case, 85 × 6 = 510) columns. Also note that the *K* locations need not be the same for all variables, hence we can freely mix atmospheric variables on a coarse horizontal grid, regional variables on a fine horizontal grid, and boundary variables along a section. This is in fact one of the major advantages of using EOF dimensional reduction as a first step in the multivariate analysis. A "stacked set" of the (dimensionless, unit-variance) time series $\mathbf{T}^{ij}$, which concatenates the rows containing the time modes of all of the *ij* entries then takes the form $\boldsymbol{T}_{(ijn)l}$ (a matrix with *I*x*J*x*N* rows and *L* columns). As in H19, we apply a second decomposition to the multivariate set of time series $\boldsymbol{T}_{(ijn)l}$. Before doing so, we multiply each series $\boldsymbol{T}_{(ijn)l}$ by the fractional variance $\boldsymbol{V}_{ijn}$ of the original signal $\mathbf{U}^{ij}$ captured by EOF mode *n*, and construct a scaled set $\boldsymbol{T}'_{(ijn)l}$ which includes all variables *i*, all months *j*, and all modes *n* associated with the original series (hence it has *I*x*J*x*N* rows and *L* columns). We decompose this new set of time series into a set of "multivariate modes" (each with one value per variable-month-univariate mode *ijn*) and "time" modes (each with one value per ESM/SSP/year *l*):

$$\boldsymbol{T}_{(ijn)l}{}' = \boldsymbol{T}_{(ijn)l}\boldsymbol{V}_{(ijn)} = \boldsymbol{M}_{(ijn)m}{}^{*}\boldsymbol{Z}_{ml} \tag{2}$$

where *m* = 1,...number of independent multivariate modes (*M* = min (*I*x*J*x*N*,*L*))

Stated another way, we have performed Principal Component analysis on the set of time series $\boldsymbol{T}_{(ijn)l}$', to summarize the covariance across variables and months. The scaling by $\boldsymbol{V}$ ensures that the multivariate modes concentrate on those spatial patterns which describe the bulk of the spatiotemporal variance in the original series; as a result, only the top few univariate modes are likely to contribute substantially to the final, multivariate result. This further decomposition yields a set of "factor loadings" $\boldsymbol{M}$ and a set of "master" time series $\boldsymbol{Z}$ modulating those spatial patterns which co-vary across the different variables and months within a single year. In fact each set of rows $\boldsymbol{M}^{ij}$ constitutes an additional rotation of each $\mathbf{X}^{ij}$ into a new set of multivariate modes $\boldsymbol{X}^{ij}$:

$$\mathbf{U}_{kl}{}^{ij} = \mathbf{X}_{kn}{}^{ij}{}^{*}\mathbf{T}_{nl}{}^{ij} = \mathbf{X}_{kn}{}^{ij}{}^{*}[(\boldsymbol{M}_{nm}{}^{ij}{}^{*}\boldsymbol{Z}_{ml})/\boldsymbol{V}_{n}{}^{ij}] = (\mathbf{X}_{kn}{}^{ij}{}^{*}\boldsymbol{M}_{nm}{}^{ij}/\boldsymbol{V}_{n}{}^{ij})^{*}\boldsymbol{Z}_{ml} = \boldsymbol{X}_{km}{}^{ij}{}^{*}\boldsymbol{Z}_{ml} \tag{3}$$

and the new spatial patterns $\boldsymbol{X}$ now strongly emphasize that portion of the original set **U** which covaries across the different variables and months. In theory, the spatial patterns $\boldsymbol{X}$ could be substantially different from the original univariate patterns **X**, depending on how strongly any secondary modes of the univariate EOFs contribute to the co-variability among the variables. Because the $\boldsymbol{Z}$s are mutually orthogonal, we can obtain the $\boldsymbol{X}$ simply by convolving **U** with $\boldsymbol{Z}$ through time:

$$\mathbf{U}_{kl}{}^{ij}{}^{*}\boldsymbol{Z}_{ml}{}^{T} = \boldsymbol{X}_{km}{}^{ij}{}^{*}\boldsymbol{Z}_{ml}{}^{*}\boldsymbol{Z}_{ml}{}^{T} = \boldsymbol{X}_{km}{}^{ij} \tag{4}$$

It is important to note here that for a single *ij* the $\boldsymbol{X}$ are not themselves mutually orthogonal; nonetheless, eq (3) shows how $\boldsymbol{X}^{*}\boldsymbol{Z}$ still completely reconstructs the original data. In practice, we use only the top 10 of the N time modes, which captures nearly all of the variance in each series $\mathbf{U}^{ij}$.

In the present context, the derived set of spatial patterns $\boldsymbol{X}$ with associated time amplitudes $\boldsymbol{Z}$ provide a summary of how the regional model plus global forcing behave - leading modes will show how particular variables covary and the spatial pattern of that covariance, and how the amplitude of those patterns changes year by year. These multivariate covariance patterns can further be used to approximate the behavior of the regional variables in **U** given a new set of global forcings **F** which span only a portion of the variables contained in **U**. For example, we may wish to use a limited set of atmospheric forcing variables from a global model, to infer the full multivariate response of the

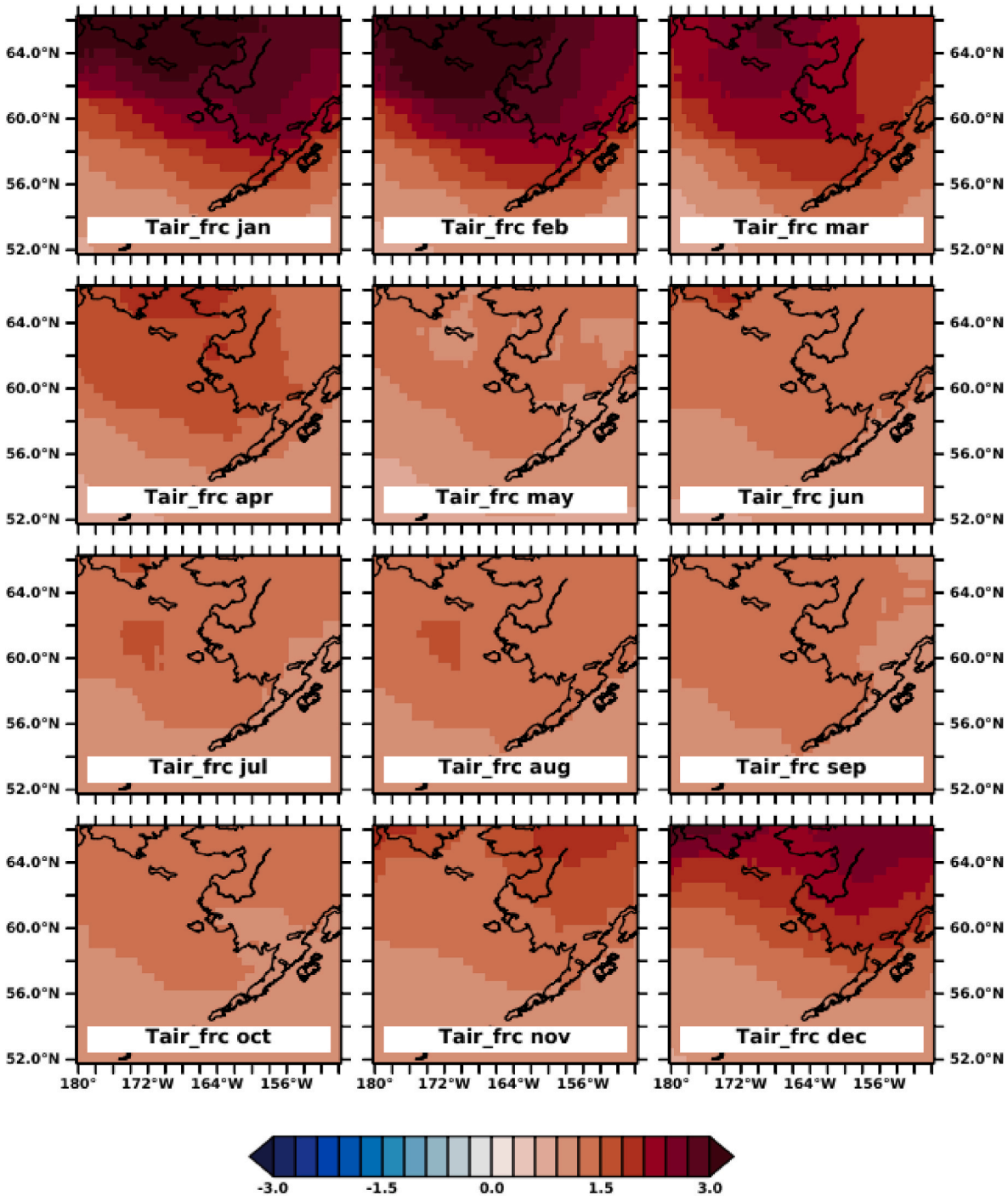

Fig. 7. Covarying monthly spatial patterns of change in air temperature (Tair_frc, in deg C).

regional model subject to that atmospheric forcing. We do this by projecting **F** onto $\boldsymbol{X}$, to estimate the time amplitudes $\boldsymbol{Y_{ml}}$. Because the $\boldsymbol{X}$ are not mutually orthogonal, we need to account for their covariance in this projection. For a single forcing variable i available for all months *j*, we use

$$\boldsymbol{C}^{\mathbf{i}}{}_{\mathbf{mm}} = \boldsymbol{X}^{\mathbf{i}}{}_{\mathbf{(jk)m}}{}^{\mathbf{T}} * \boldsymbol{X}^{\mathbf{i}}{}_{\mathbf{(jk)m}} \tag{5}$$

$$\boldsymbol{Y}_{\mathbf{pl}} = \boldsymbol{X}^{\mathbf{i}}{}_{\mathbf{(jk)p}}{}^{\mathbf{T}} * \mathbf{F}^{\mathbf{i}}{}_{\mathbf{(jk)l}} / (\boldsymbol{C}^{\mathbf{i}}{}_{\mathbf{mp}}{}^{\mathbf{T}} * \boldsymbol{C}^{\mathbf{i}}{}_{\mathbf{mp}}) \tag{6}$$

where $\boldsymbol{C}^{\mathbf{i}}{}_{\mathbf{mp}}$ refers to the *p*th column of $\boldsymbol{C}^{\mathbf{i}}{}_{\mathbf{mm}}$ and the (*jk*) rows refer to all the month-locations where we have available data for forcing variable *i*.

In the present case, based on the observed covariance structure of the dynamically downscaled results, we chose air temperature as our forcing variable $\mathbf{F}^{\boldsymbol{i}}$. A full set of spatially gridded air temperatures was obtained from over 40 different IPCC modeling center realizations under scenarios SSP126 (Table 3) and SSP585 (Table 4); in some cases these included multiple realizations of the same model. Each global model realization of $\mathbf{F}^{\boldsymbol{i}}$ was used to derive a modulating series $\boldsymbol{Y}$ and ultimately a "statistical downscaling" estimate of the resulting **U**, here denoted by $\boldsymbol{U}$:

$$\boldsymbol{U}_{\mathbf{kl}}{}^{\mathbf{ij}} = \boldsymbol{X}_{\mathbf{km}}{}^{\mathbf{ij}} * \boldsymbol{Y}_{\mathbf{ml}} \tag{7}$$

For the three dynamically downscaled models (GFDL, MIROC, CESM), the dynamical and statistical results (that is, $\mathbf{U}_{\mathbf{kl}}{}^{\mathbf{ij}}$ vs $\boldsymbol{U}_{\mathbf{kl}}{}^{\mathbf{ij}}$) were

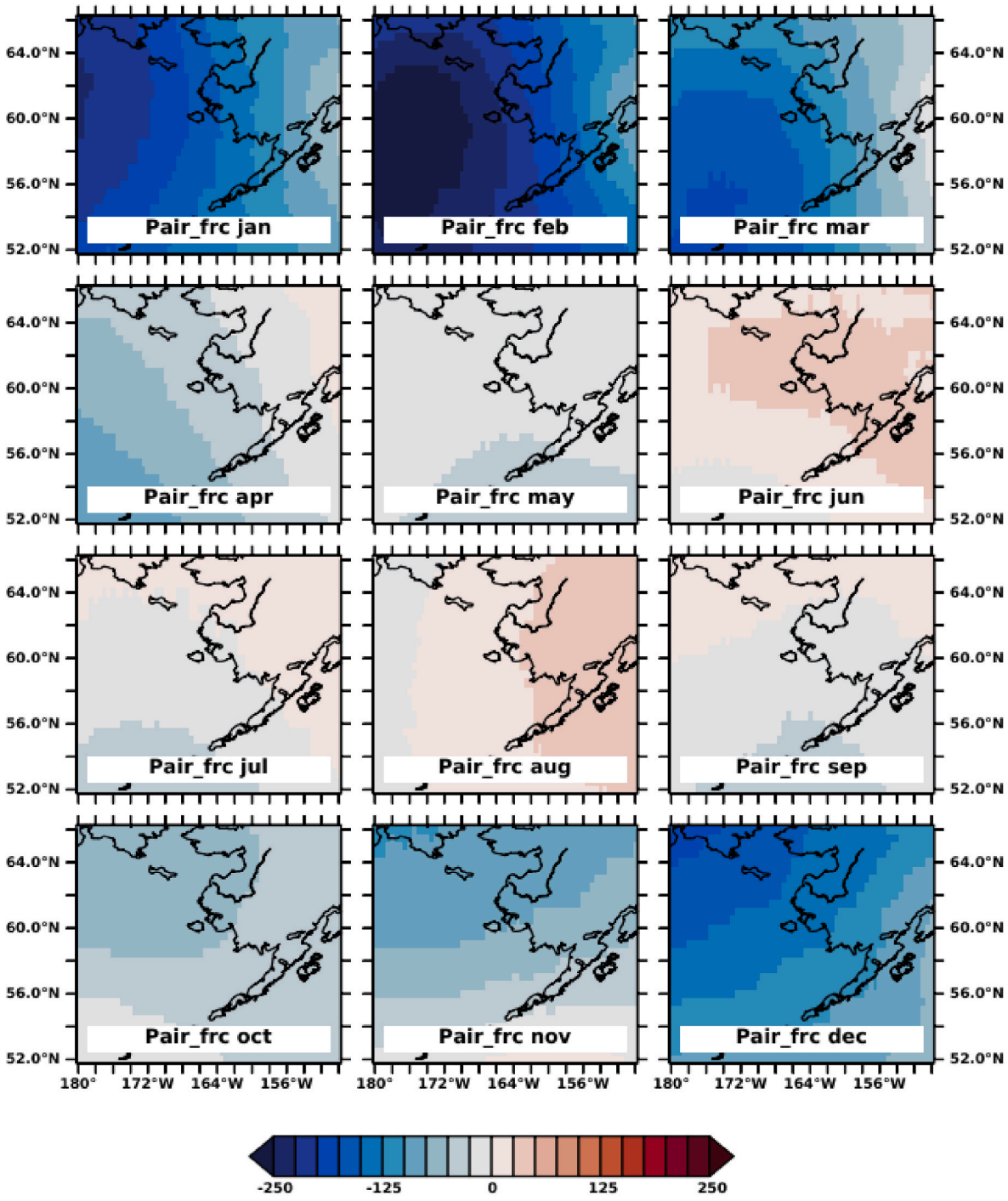

Fig. 8. Covarying monthly spatial patterns of change in air pressure (Pair_frc, in Pa).

compared for July bottom temperatures and depth-integrated shelf Euphausiids, as a rough check of the method. Subsequently the method was used for statistical estimates of downscaled ensemble mean changes in these two properties between 2015 and 2100 under the two different emission scenarios.

To summarize the spatial results for each variable and month, and the relative shifts in phenology, we spatially averaged the leading multivariate modal amplitudes X over six subregions of the shelf, following subdivisions based on the biophysical domains of the Bering Sea shelf. These are the same domains as are used in the results of C21. These subdivisions separately span the inner (0–50m), middle (50–100m) and outer (100–200m) shelf domains, in both southern (54N–60N) and northern (60N–64N) regions. For each of the variables, the spatial averages for each subdomain are then displayed on the same graph as a function of month.

We further calculate the average fractional variance explained by the leading multivariate mode for each variable and month, where the average is taken over the full domain used in calculating the monthly anomalies (and the subsequent univariate EOFs). We also calculate the frequency spectra of the "master" time series Z, doing this separately for each of the downscaled realizations that were used in the concatenated anomaly series.

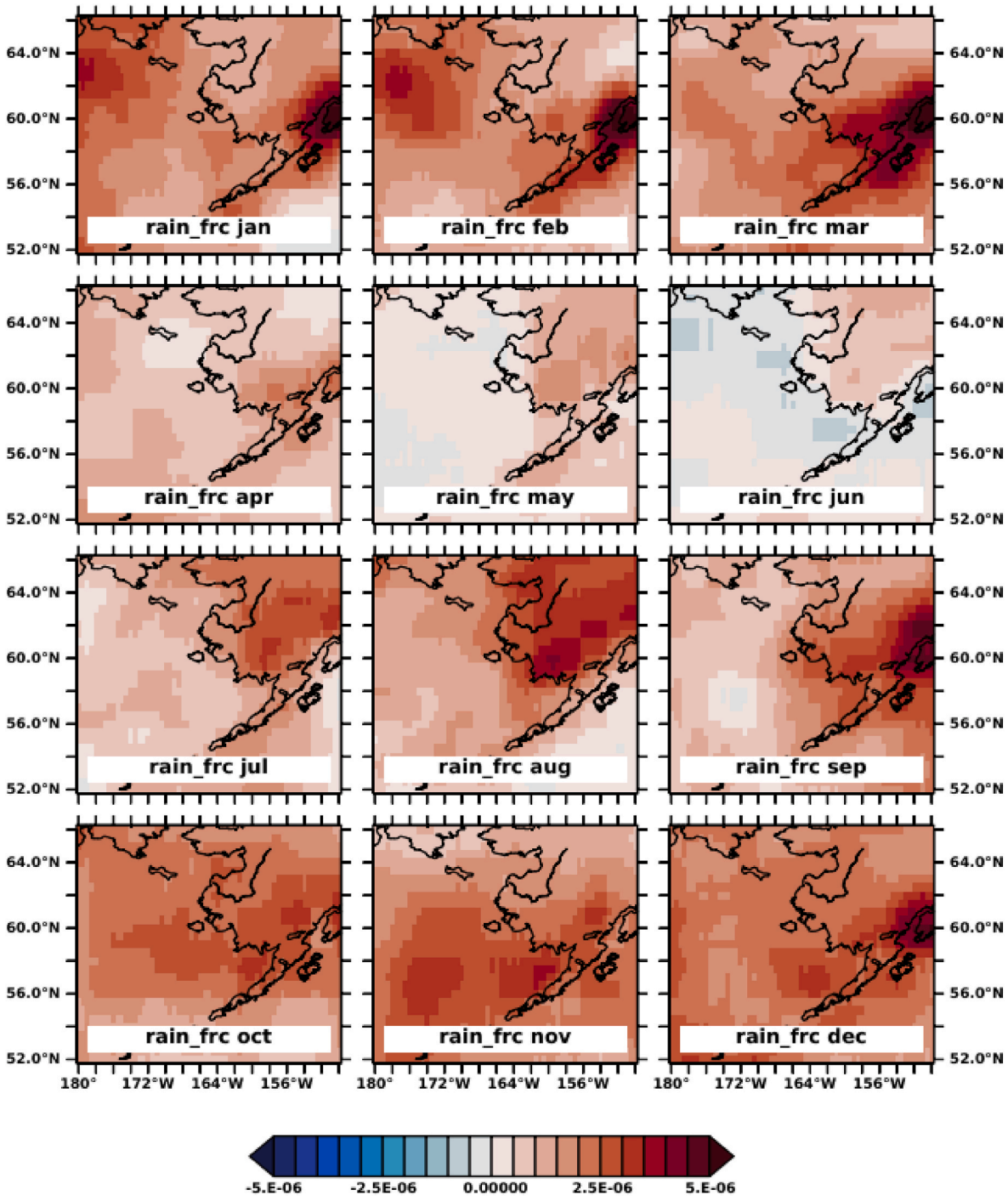

Fig. 9. Covarying monthly spatial patterns of change in rainfall (rain_frc, in m s^{-2}).

3. Results

An examination of the full matrix **M** revealed that only the leading univariate EOFs, modulated by the scaled set **T′**, made a significant contribution to the leading multivariate mode, or to any of the lesser multivariate modes. In the following we focus on the leading multivariate spatial modes, how they covary across different variables and months. Since in our case only the leading univariate modes were significant contributors to the multivariate mode, the univariate and multivariate spatial patterns are in fact similar, but with different overall amplitudes.

3.1. Dominant pattern of covariance across variables and months

A summary map of the "factor loadings" for each variable during each month is shown in Fig. 3 (this is essentially that portion of the matrix **M** corresponding to the leading univariate modes). Since spatial modes **X** from univariate EOF analysis can have both positive and negative values depending on location, for clarity we flipped the signs of the univariate spatial patterns **X** (and their corresponding time series **T**) to be spatially-averaged positive prior to calculating **M**. For example, in Fig. 3, a positive value for temperature and a negative value for nitrate indicates that the (spatially averaged positive) univariate EOF for temperature was positively covariant with the multivariate mode, and the

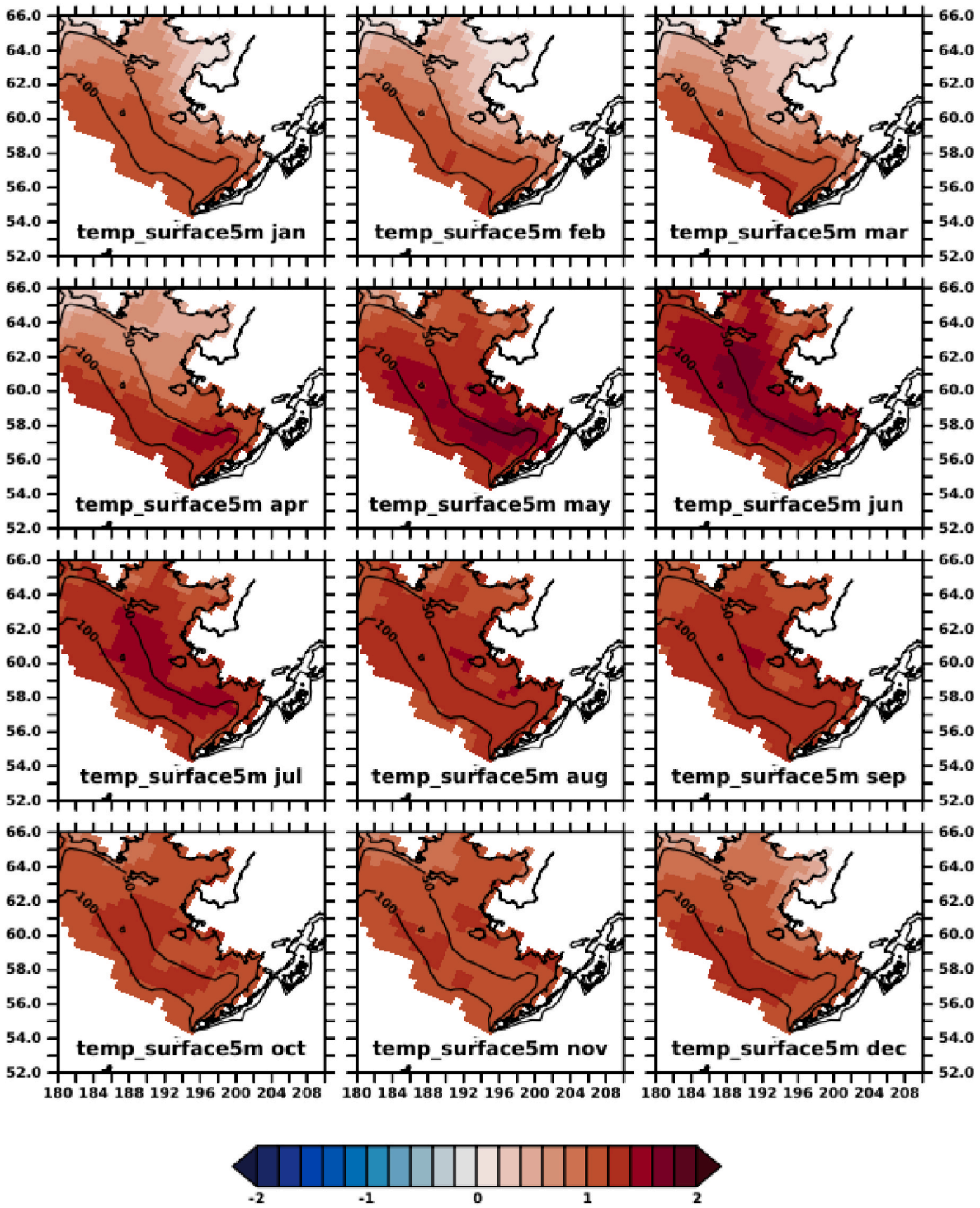

Fig. 10. Covarying monthly spatial patterns of change in ocean surface temperature (temp_surface5m, in deg C). Light red shading indicates regional model domain. For ocean surface, bottom, and depth-integrated variables, the statistical analysis is restricted to output from the Bering Sea continental shelf (depth 0–200m).

(spatially averaged positive) univariate EOF for nitrate was negatively covariant with that multivariate mode. The detailed spatial patterns of the primary multivariate mode, obtained through the convolution shown in eq (6), will be displayed in subsequent figures.

Fig. 3 indicates a strong connection among the monthly anomalies of certain variables and months; in this figure, correlated darker colors indicate that the particular spatial patterns of anomalies for those variable-months (which may in fact be very different for each variable-month) tend to occur together in our yearly samples. In particular, for the first mode it is observed that warmer air temperatures, absolute humidity, downward longwave radiation, and ocean temperatures (both top and bottom) are strongly linked with reduced ice area, ice thickness and salinity. Among the biological variables linked with these physical changes are a drop in nitrate and a shift in the phenology to earlier blooms and earlier decay of phytoplankton and zooplankton. A shift is indicated by increased amplitude of the spatial pattern earlier in the year and decreased amplitude of the spatial pattern later in the year. This phenological shift is arrayed "trophically" in the figure, with an

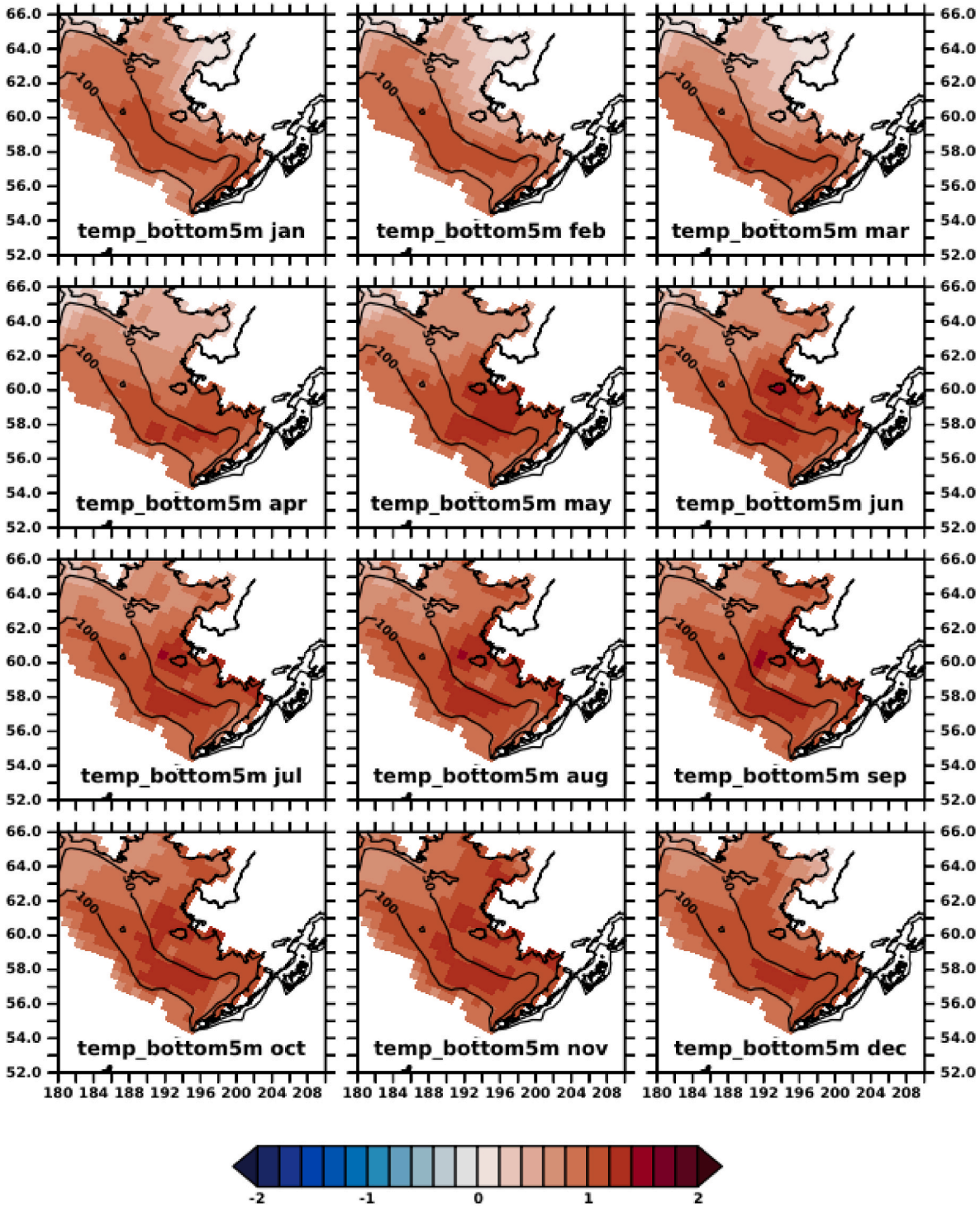

Fig. 11. Covarying monthly spatial patterns of change in ocean bottom temperature (temp_bottom5m, in deg C).

earlier shift in phytoplankton, later shifts in zooplankton, and the latest shift in jellyfish. In addition, by the fall, lower mean values of large copepods are consistently associated with the spatially-averaged warmer temperatures.

The spatially averaged fractional variance of the original, full time series explained by the leading two multivariate modes is shown in Fig. 4. Note the strong similarity of this plot to the modal amplitudes of Fig. 3.

The leading multivariate mode time series **Z** modulating the leading mode factor pattern is shown in Fig. 5, here broken apart into the original six downscaling simulations that were used to construct the concatenated series of yearly samples. This figure indicates how the amplitude of the shared multivariate pattern changes over the 21st century in each dynamically downscaled realization. For each of the three global models, the SSP585 run exhibits a larger difference between the beginning and end of the simulated period than the SSP126 run of that model. Co-varying patterns of change are larger (on average, approximately 4x greater) under SSP585 than under SSP126 near the end of the 21st century (~2080–2100). For the SSP585 runs especially, there is a low-frequency trend (associated with warming, as detailed

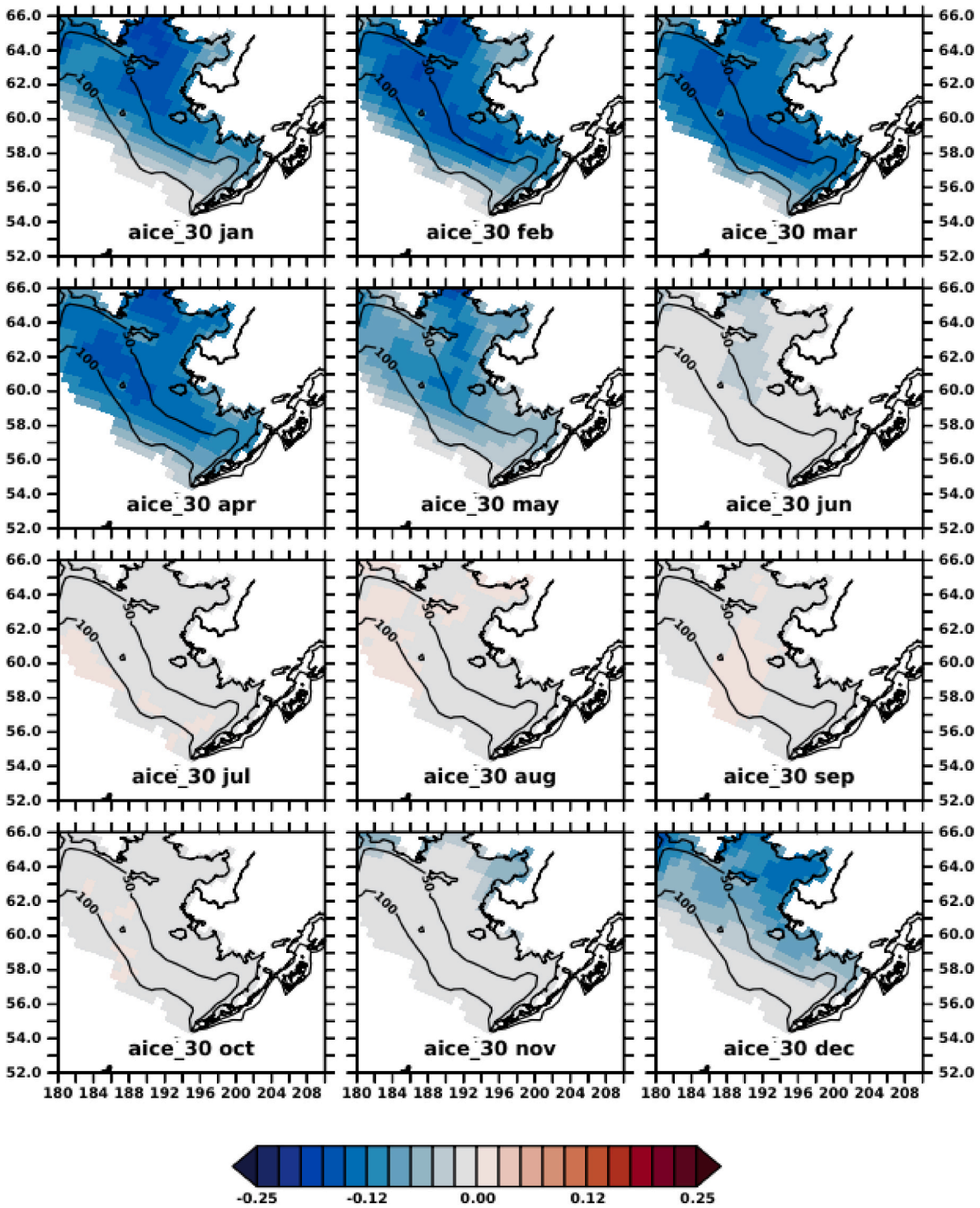

Fig. 12. Covarying monthly spatial patterns of change in areal ice cover (aice_30, in fractional area).

below), as well as strong decadal and interannual variability throughout the 21st century. More specifically, the time series of this leading mode for SSP585 have "red" spectra, with secondary peaks at decadal-to-interannual scales.

The second multivariate mode amplitudes are focused on biological changes in the winter, apparently uncorrelated with physical changes or forcing terms (Fig. 3). While the time series associated with this mode have far whiter spectra than the leading mode, the GFDL results stand out, with large secondary peaks in the 5–10 year range (Fig. 6).

3.2. Spatial modes by variable and month

We now examine monthly spatial patterns associated with the leading multivariate mode, focusing especially (but not exclusively) on those which load most strongly on that leading multivariate mode. A full set of these leading multivariate spatial patterns is included in Appendix, arranged in the same order as Table 2 and Fig. 3. Generally speaking, given the modulating time series in Fig. 5, when we refer to a "positive" pattern, it indicates the pattern of change between the start and end of the 21st century projections. The actual yearly time series of the

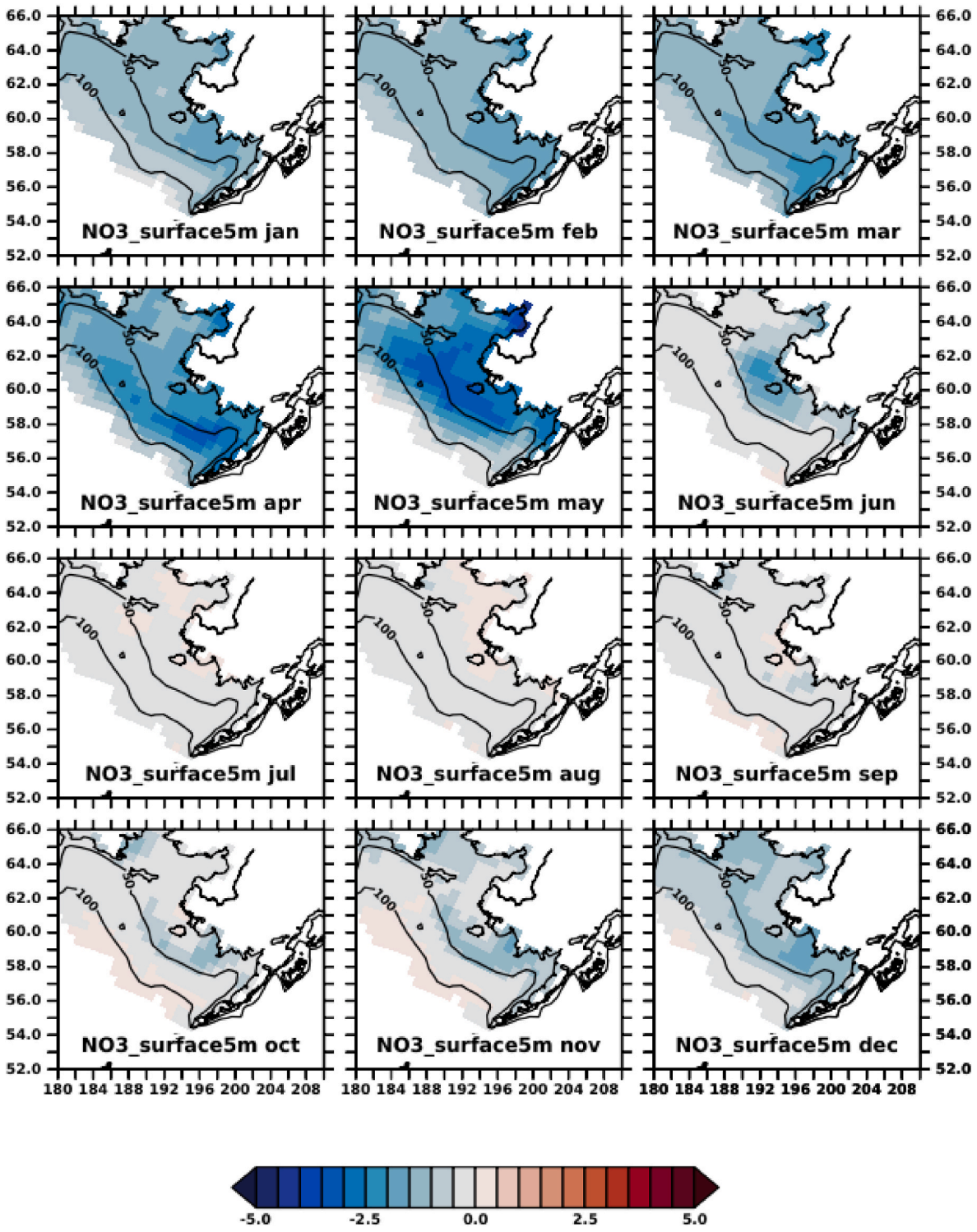

Fig. 13. Covarying monthly spatial patterns of change in ocean surface nitrate (NO3_surface5m, in mmol N m^{-3}).

covarying change, relative to the full 21st century climatology of a particular downscaling simulation, is in fact this pattern multiplied by the values of the modulating time series shown in Fig. 5.

3.2.1. *Atmospheric variables*

The spatial pattern of air temperature is positive, concentrated in Dec–Mar, and focused on the northern Bering Sea (Fig. 7). A similar spatial pattern is observed for downward longwave radiation (see Appendix). Spatially broad positive covarying changes in absolute humidity are strongest in the summer months (see Appendix). The spatial pattern for shortwave radiation changes from negative (less incident shortwave radiation) in spring to positive (more incident shortwave radiation) in summer (see Appendix), and like air temperature, tends to be focused on the northern Bering Sea. Presumably this derives in part from increased cloud cover in the ESM results, which is associated with both reduced downward shortwave and increased downward longwave radiation at the ocean surface; more analysis would be needed to quantify the relative contributions of cloud cover vs

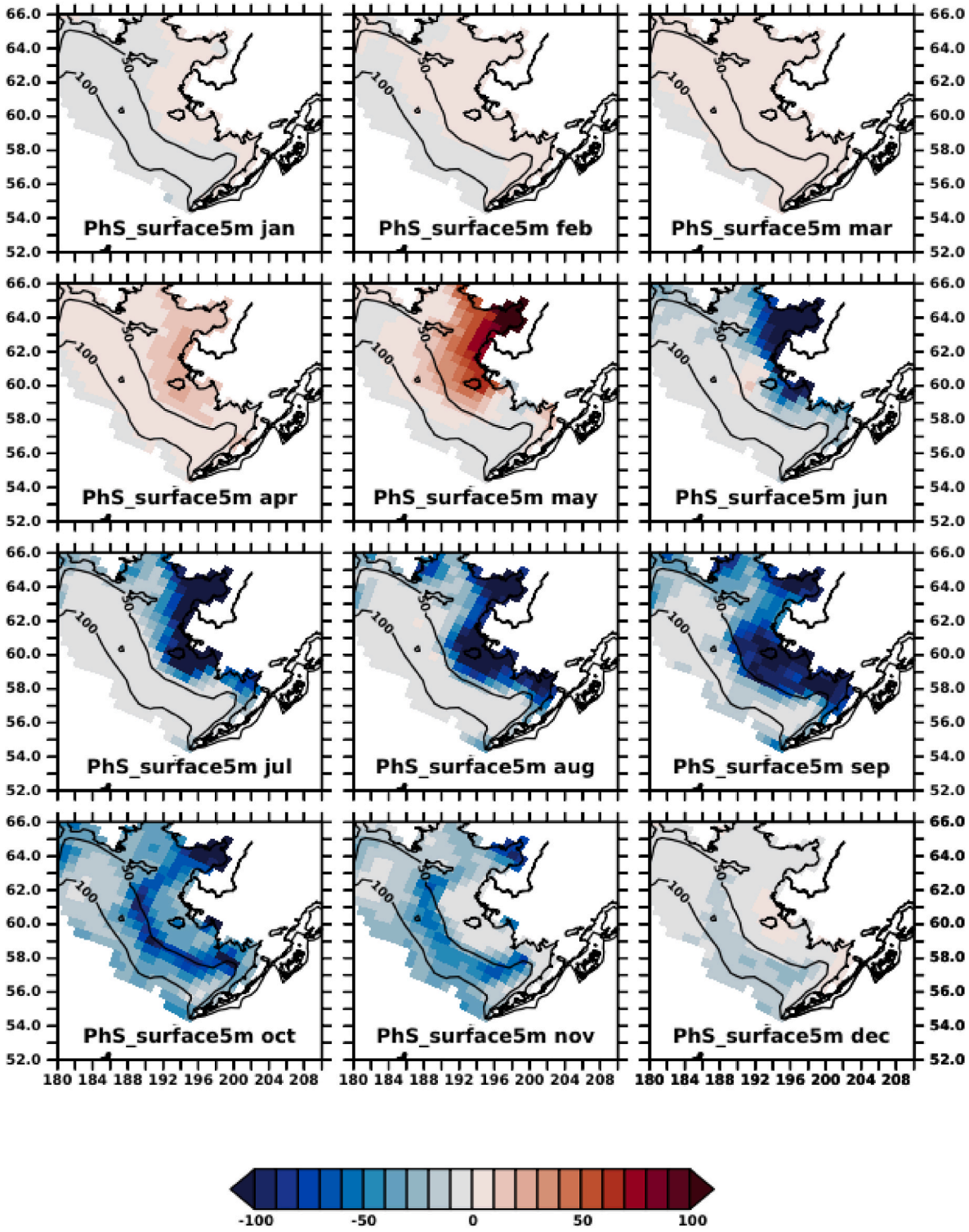

Fig. 14. Covarying monthly spatial patterns of change in ocean surface small phytoplankton (PhS_surface5m, in mg C m^{-3}).

temperature to the longwave total. Air pressure and wind changes are concentrated in the winter months, and indicate a tendency towards northeastward wind stress in the future (Fig. 8). The precipitation pattern is weakest in May–June, and shows enhanced winter precipitation in the Gulf of Alaska (Fig. 9).

3.2.2. *Regional ocean variables*

Among the physical variables, the ocean surface temperature pattern (Fig. 10) is positive and strongest offshore during winter, but strongest at mid-shelf in summer. The bottom temperature pattern (Fig. 11), similarly positive, is concentrated at mid-shelf throughout the year. The pattern for areal ice cover (Fig. 12), always negative, is strongest during the winter, and focused on the northern Bering Sea.

Among the biological variables, nitrate is strongly covariant throughout the year (Fig. 3), with lowest values in May (Fig. 13). Small surface phytoplankton have a positive pattern in May (focused in Norton Sound) and negative patterns thereafter which gradually shift from the inner to the middle shelf during Jun–Oct (Fig. 14). Integrated shelf

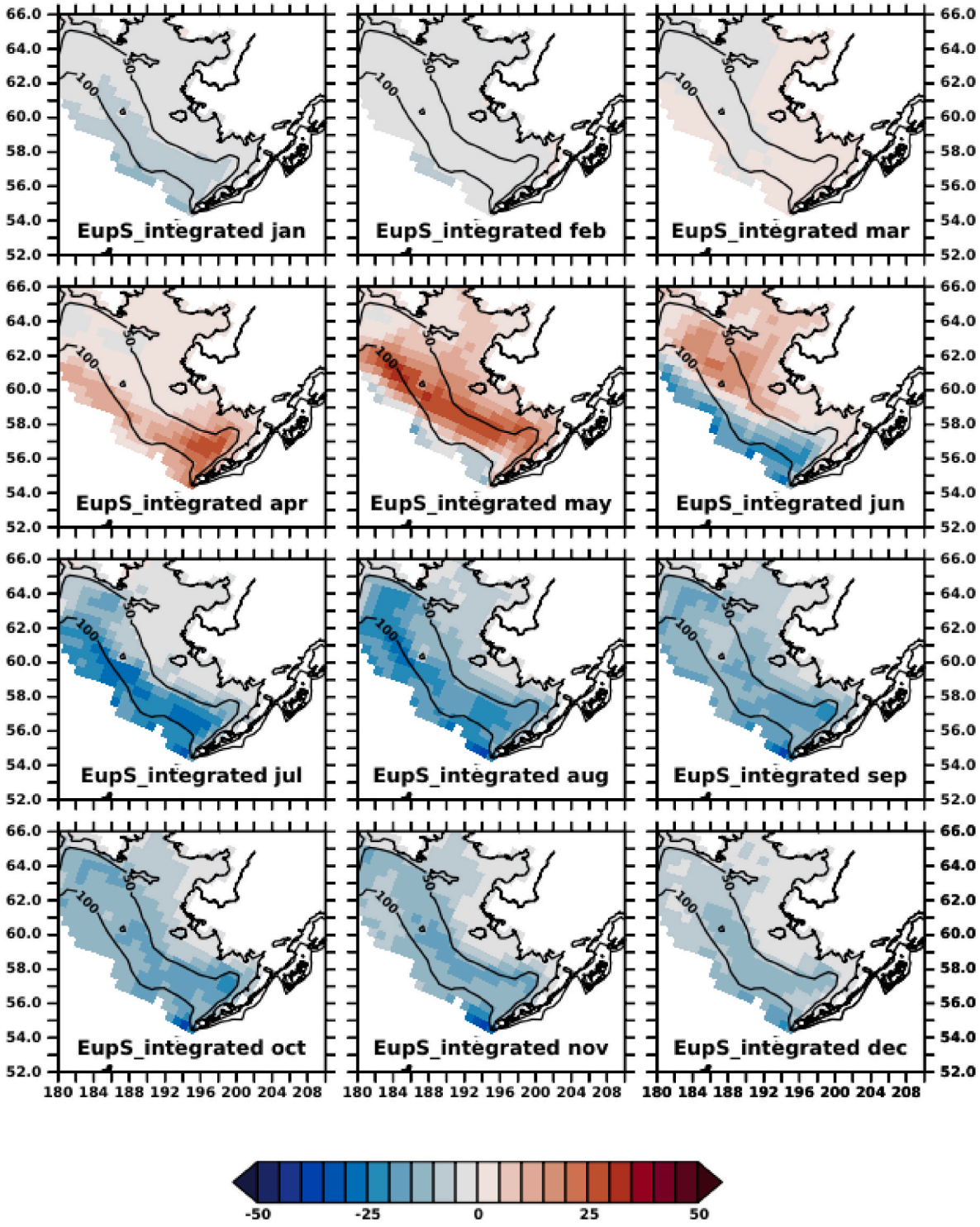

Fig. 15. Covarying monthly spatial patterns of change in depth-integrated on-shelf euphausiids (EupS_integrated, in mg C m^{-2}).

euphausiids exhibit a positive pattern on the outer shelf in April which shifts onshore through June; during July–Dec the pattern is negative (Fig. 15).

Subdomain-averaged summaries of the full set of variables is plotted in Figs. 16–18, for the forcing and boundary conditions (Fig. 16), the regional physical variables (Fig. 17) and the regional biological variables (Fig. 18). The pattern of freshening for salinity is strongly focused on Norton Sound (see Appendix) and strongest during Dec–May (Fig. 17). A tendency towards greater surface "cross-shelf" and "along-shelf" velocities is evident in the winter months (Fig. 17), corresponding to the period of greatest change in air pressure and winds (Fig. 16). As noted in the methods, "cross-shelf" and "along-shelf" are here approximated by the native coordinate system of the ROMS model shown in Fig. 1, which runs roughly southwest to northeast and southeast to northwest, respectively. Hence positive "cross-shelf" flow indicates flow towards the northeast, and positive "along-shelf" flow indicates flow towards the northwest. The large surface phytoplankton exhibit both positive and negative areas during April and May (see Appendix), and are dominated by a negative pattern which shifts inshore during Jun–Jul (Fig. 18). Surface microzooplankton exhibit a positive pattern in the

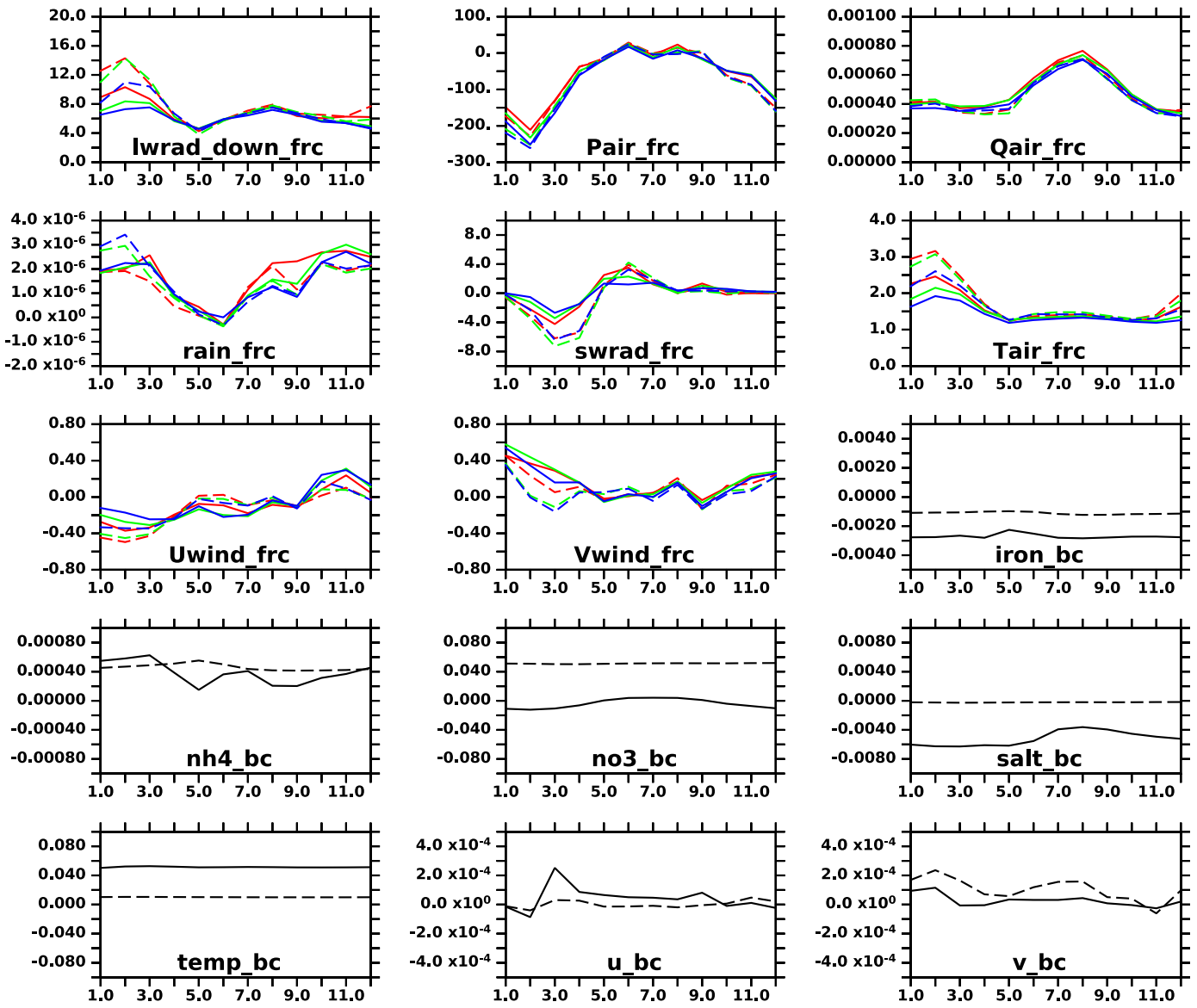

Fig. 16. Areal averages of the leading multivariate mode spatial patterns, taken over subdomains of the continental shelf by month (abcissa), for atmospheric forcing and ocean boundary conditions. See Fig. 1 for spatial domains and Table 2 for units. For the atmospheric forcing, domains plotted are for the inner (red), middle (green) and outer (blue) shelf, in the southern (solid) and northern (dashed) regions. For the boundary conditions, a line average of southeastern (solid) and northwestern (dashed) results are shown. Full maps of each variable are provided in the Appendix.

southeast in April, which shifts north in May–June (Fig. 18). The pattern in June is positive nearshore and negative at mid-shelf, and is generally weaker thereafter. Surface copepods exhibit a similar pattern to surface microzooplankton, but with stronger negative patterns in July–Dec (Fig. 18). Integrated jellyfish exhibit a positive pattern at the shelf break in May–Jun which shifts onshore during July–Aug, and a negative pattern focused at the shelf break during Oct–March (Fig. 18).

3.3. Statistical projection of regional model behavior using multivariate modes

As in H19, these multivariate modes can be used to project the approximate behavior of the regional model under a broad suite of global ESM forcing. As with CMIP5, it was found that a few of the forcing variables - and air temperature over the Bering Sea in particular - should exert a large influence on these projections. Once obtained, this larger ensemble may be useful in Management Strategy Evaluations (Punt et al., 2016), where a large ensemble of realizations is desirable to properly capture uncertainty (Hollowed et al., 2020).

In Fig. 19, we take air temperatures by month from the three models used in dynamical downscaling, and project them onto the multivariate modes as in eqs (6) and (7) to obtain estimates of July bottom temperatures. These are compared with the original, dynamically downscaled results. Essentially we are examining here how much of the mean change and spatial pattern we can replicate using our statistical approach, based on those few downscaled runs. Specifically we look at the 30-year mean pattern change from 2014-2044 to 2070–2099. Warming exceeds 1 degree C in all areas; for two of three dynamically downscaled models, the greatest change is focused on the outer northern shelf. The patterns are strikingly similar between dynamical and statistical methods for the MIROC model, and highly similar for the CESM model as well. The GFDL model exhibits the greatest difference between methods, but nonetheless includes warming of the outer northern shelf under both methods.

In Fig. 20, we present the full results of the statistical downscaling for July bottom temperatures on the shelf, using a broad array of over 40 global models under emission scenarios SSP126 and SSP585. As in

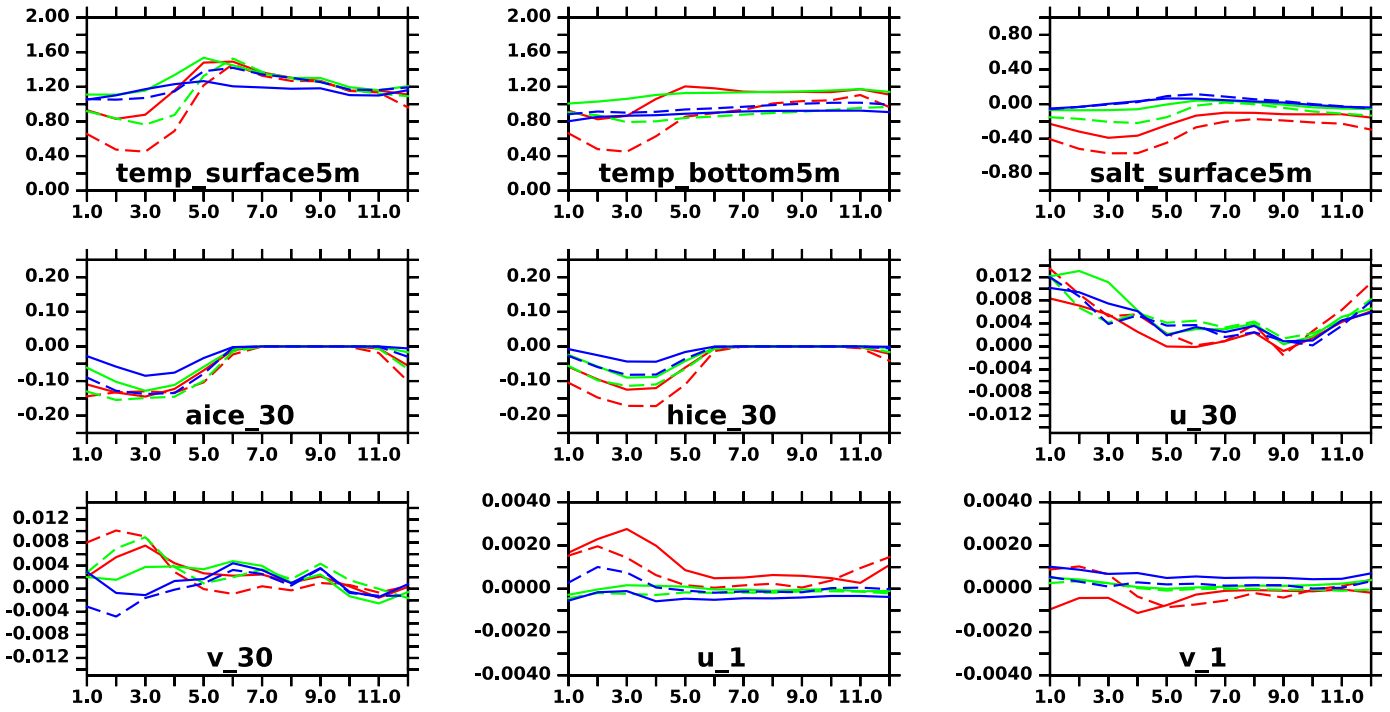

Fig. 17. Areal averages of the leading multivariate spatial modes for the regional model physical variables, by subdomain and month (abcissa). See Fig. 1 for spatial domains and Table 2 for units. Domains plotted are for the inner (red), middle (green) and outer (blue) shelf, in the southern (solid) and northern (dashed) regions.

Fig. 19, we exhibit the 30-year mean pattern change from 2014-2044 to 2070–2099, and find that the ensemble mean pattern is strongest on the northern outer shelf. Warming in parts of this area exceeds 5 degrees C under SSP585. We further show the annual time series of monthly average July shelf bottom temperatures under each of these emission scenarios. Note how the ensemble mean rise in temperature is ~4 degrees C under the low carbon mitigation (i.e. high emission) scenario (SSP585), as compared with ~1 degrees C under the high carbon mitigation (i.e. low emission) scenario (SSP126). A companion set of figures for July depth-integrated Euphausiids (Figs. 21 and 22) projects strongest declines on the outer shelf, in excess of 75 gC m^{-2}. As with bottom temperatures, the largest discrepancies between the dynamical vs statistical method are observed for the GFDL case. The ensemble mean decrease is ~50 gC m^{-2} under SSP585, as compared with ~12 gC m^{-2} under SSP126. One key feature of these ensemble means is that bottom temperatures and zooplankton both stabilize at new equilibria after 2060 under SSP126, whereas this does not occur in the next 85 years under SSP585.

4. Discussion

4.1. Interpreting the patterns

Some of the most striking patterns revealed by this analysis are: 1) a strong correlation of many regional biophysical properties with the forcing temperature, absolute humidity and downward longwave radiation; 2) reduced nitrate is associated with warming throughout the year; 3) warming drives a phenological shift in plankton, with time lagged effects from phytoplankton to zooplankton to jellyfish; 4) warming leads to reduced values of large zooplankton in the late summer and fall. Several of these patterns were found in the multivariate analysis of downscaled CMIP5 results in H19, which were based on annual averages over the entire eastern Bering Sea, and used an earlier version of the NPZ model. The present work, as it includes patterns by month, reveals the phenological detail of these changes and clarifies how they shift through time across the shelf. Several of the emergent patterns are similar to the changes in univariate monthly climatologies between 1980-2014 and 2066–2100, described in C21. However, as demonstrated in Fig. 4, the covariant patterns apply not just to the gradual multidecadal trends, but to the interannual variability as well. We consider each of these patterns as follows:

1) Among the physical variables, as expected, there is a strong association between air temperature and ice. The association with winds is weaker; however, the spatial patterns are consistent with more northward (i.e. southerly) winds being associated with reduced ice cover. Under present-day conditions, winds play a substantial role in the penetration of ice to the southeastern Bering Sea (Cokelet, 2016). The strong correlation between ice and salinity patterns in Norton Sound (less salt with less ice) may be due to reduced brine rejection under warming, as well as the increased rainfall and Yukon River runoff. In addition, there is enhanced salinity on the other shelf in May–June (Fig. 11), consistent with the argument in C21 that a reduction in ice leads to a reduction in surface freshening by ice melt.
2) The association of reduced surface nitrate with warming conditions could be due to several factors. Potentially this is due to changes in stratification of the water column as discussed in C21. The bottom and boundary nitrate values decline as well; this tendency conforms to that of the ESMs themselves, as shown in C21.
3) The time-lagged shifts in phenology naturally correspond to the links in the food chain, with sequential blooms in phytoplankton, then smaller zooplankton, larger zooplankton, and finally jellyfish. Several of these phenological shifts are noted in the univariate analyses of C21. Kearney et al. (2020) has detailed the phenology of phytoplankton in the hindcast version of the K20 model used here and found a late May peak in phytoplankton biomass; our results here suggest that peak will shift to earlier by 2–4 weeks to late April or early May. The simplest explanation of the phenological shift in phytoplankton is that higher temperatures tend to advance the onset of net primary production to yield blooms earlier in the year. There may also be a substantial effect of sea ice loss, which increases solar radiation to the water column, even as it reduces the near-surface stratification associated with ice melt (but note our covarying patterns suggest a net surface freshening in the north under warming,

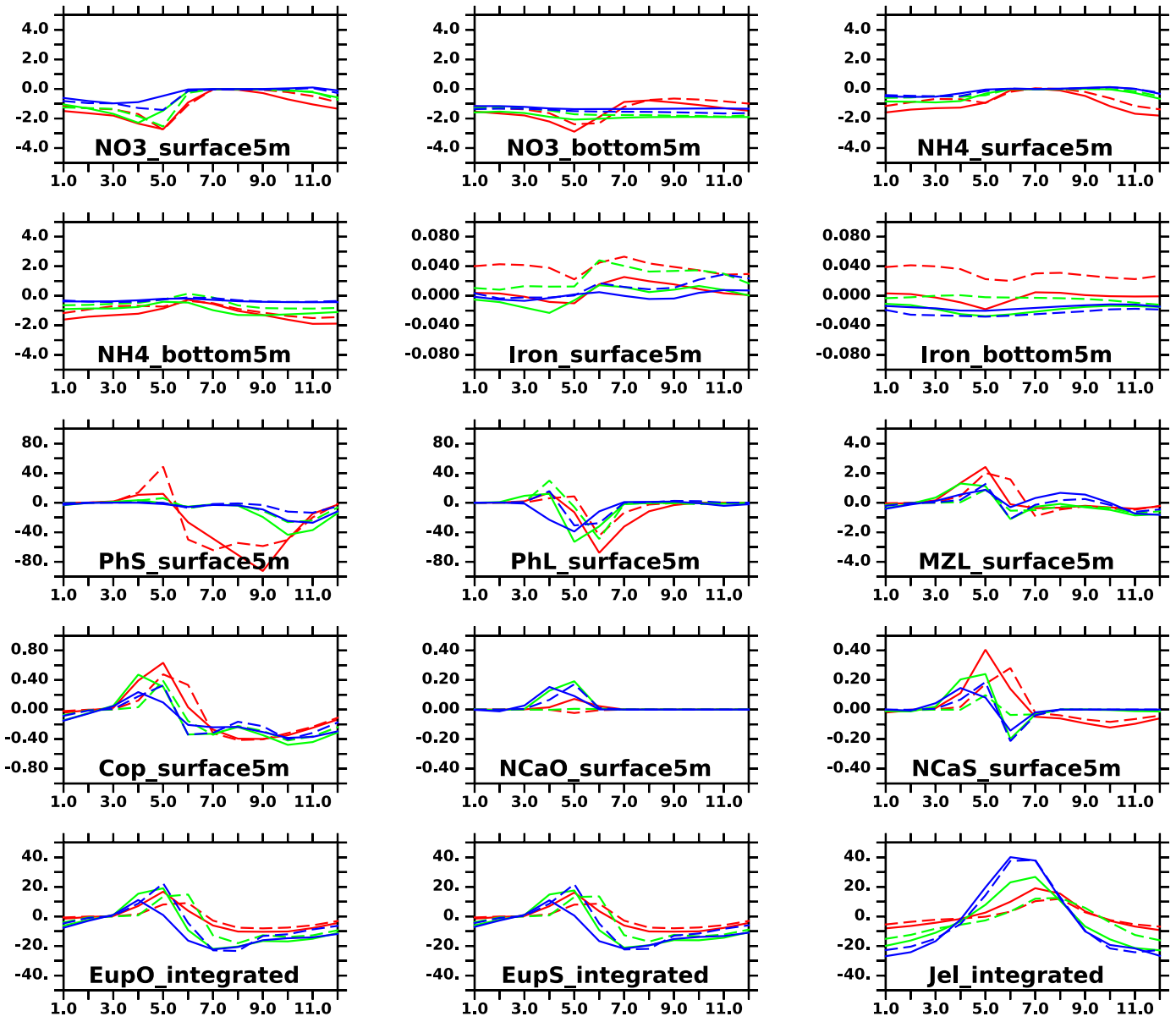

Fig. 18. Areal averages of the leading multivariate spatial modes for the regional model biological variables, by subdomain and month (abcissa). See Fig. 1 for spatial domains and Table 2 for units. Domains plotted are for the inner (red), middle (green) and outer (blue) shelf, in the southern (solid) and northern (dashed) regions.

likely due to reduced brine rejection in the winter by southward-advecting ice). The earlier zooplankton and jellyfish blooms may simply be following the earlier phytoplankton bloom, but are themselves subject to direct temperature impacts on growth rates. It is hence likely that both effects contribute to their phenological shifts.

4) In addition to reduced nitrate and primary production, the direct temperature dependence of zooplankton respiration and grazing closure terms may account for the lower overall biomass of large zooplankton in the fall under warming. This decline in fall zooplankton, similarly observed in the previous modeling results of H13 and H19, may impact fish which depend on that food source prior to overwintering (Sigler et al., 2016; Duffy-Anderson et al., 2017), with strong implications for management (Holsman et al., 2020).

In some ways these patterns conform to the findings of H19, which were based on annual rather than monthly averages. In particular, the strong association between air temperature, ice cover, and oceanic bottom temperature has been retained, with winds playing a secondary role. Whereas H19 predicted largest anticipated annual bottom temperature changes on the northern shelf, our new results suggest that for most months, the largest changes will be seen farther south. Both H19 and the new results predict an overall loss of nutrients, phytoplankton, and large crustacean zooplankton; the new results identify the seasonality (phenology) of these anticipated changes.

4.2. Secondary multivariate modes

The second multivariate mode explained far less variance of the original dataset than the first multivariate mode (Fig. 4) and strongly emphasized phenological changes in the winter months, e.g. a January increase in phytoplankton associated with February increases in zooplankton and a March increase in jellyfish. Increased surface and bottom nitrate and ammonium (as opposed to their decrease in mode 1) were covariant in mode 2, as well as, to a lesser degree, surface and bottom temperature of the regional model. Unlike mode 1, there was little contribution of any of the ESM physical variables to mode 2.

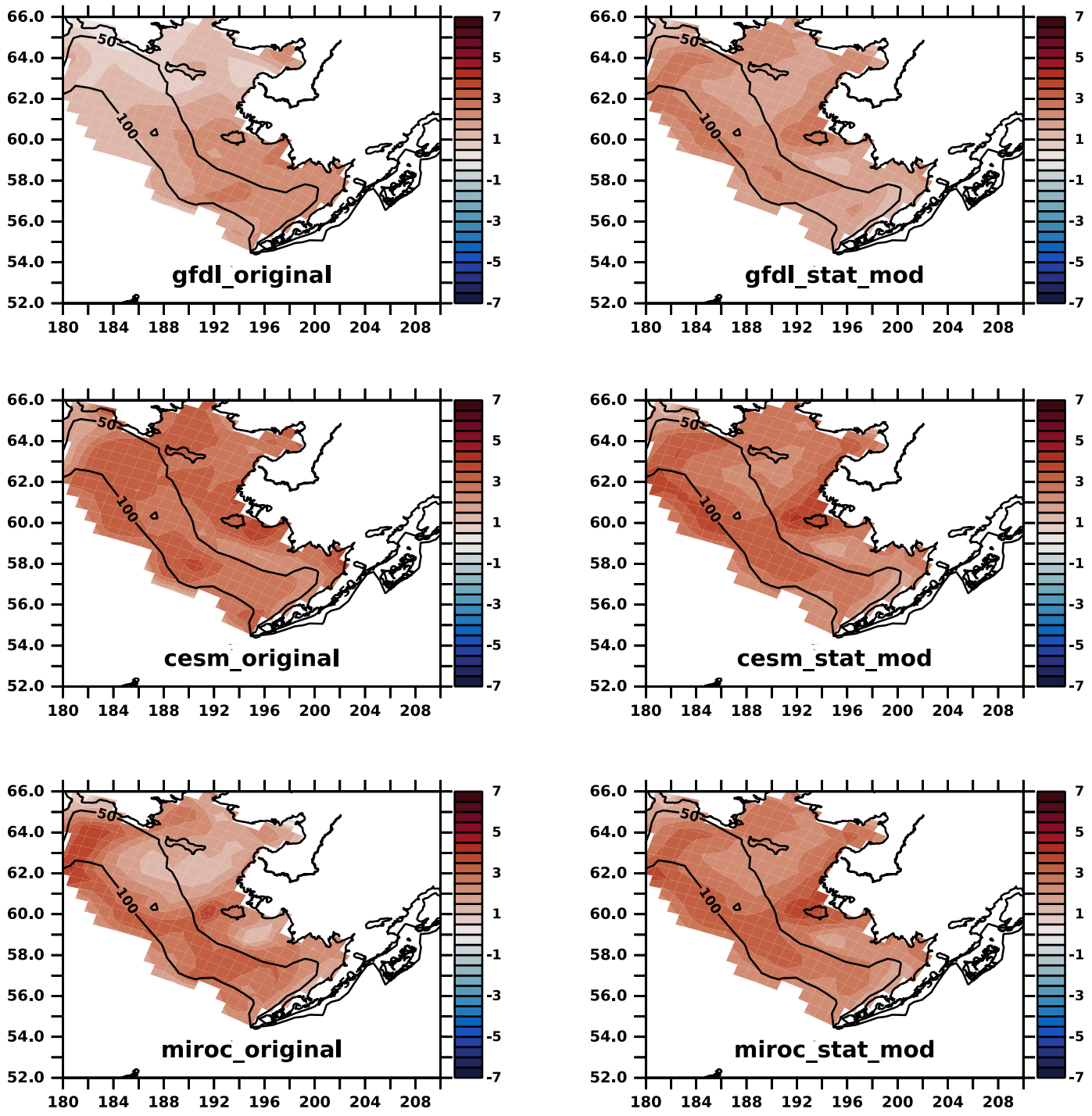

Fig. 19. Comparison of dynamically downscaled results from single global models with their "hybrid" statistical equivalent, derived using only air temperature from the global model. Shown are the projected change in 30-year average July bottom temperatures (degrees C), between 2015-2044 and 2070–2099, under SSP585.

Together these results imply this mode is primarily capturing initial adjustment and subsequent internal variability of the GFDL-forced regional model, unconnected with the interannual variability of the global atmospheric or oceanic forcing. While this mode is apparently not as useful as the leading mode for estimating the regional response to alternate global forcing, it provides an example of how the multivariate method is able to ferret out unique (here, almost purely biological) aspects and consequences of a particular forcing set.

4.3. Alternate methods

A broad overview of regional downscaling methods for earth system models can be found in Drenkard et al. (2021). Here, we focus on a few issues relevant to the specific methods used in our study.

For the dynamical downscaling, we used the global forcing and boundary conditions without bias correction. Various "delta" methods have been utilized in downscaling, which entail the addition of yearly and/or monthly changes from a coarse-scale ESM to an existing fine-scale climatology. While this approach has considerable merit in retaining fine-scale forcing gradients (e.g. in winds), it can obscure

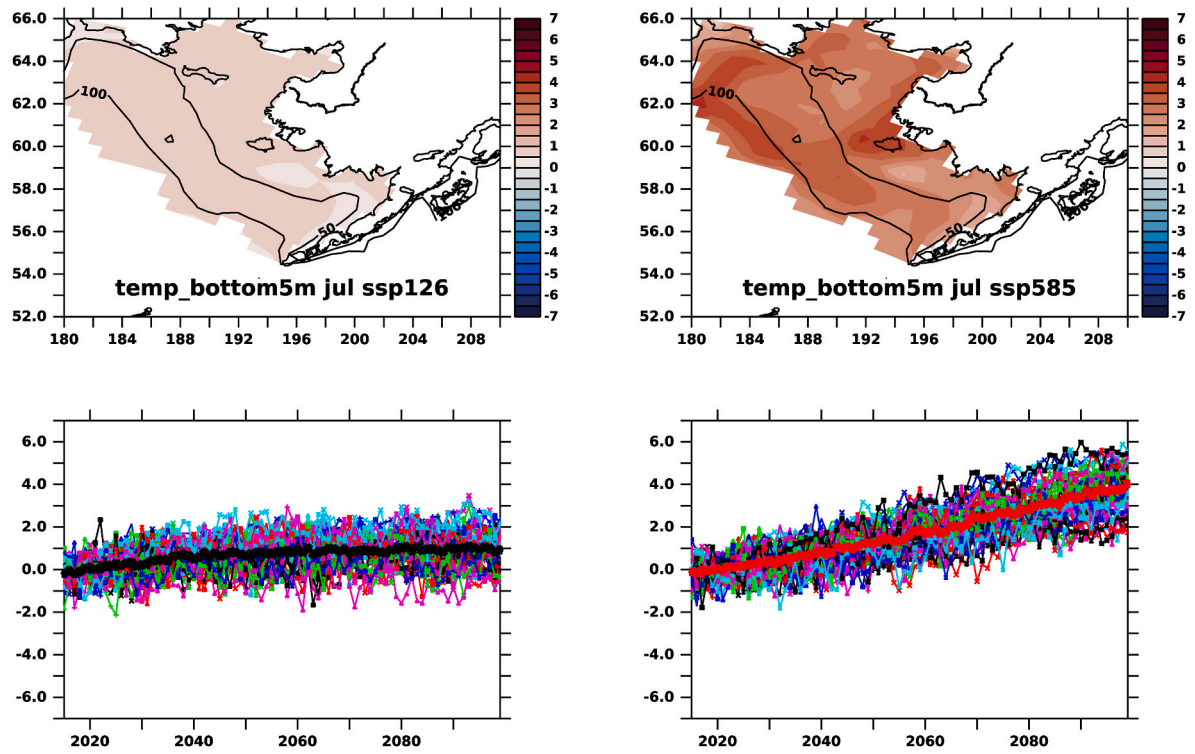

Fig. 20. Upper panels: ensemble average of projected change in 30-year average July bottom temperatures (degrees C) between 2015-2044 and 2070–2099, under SSP126 (left) and SSP585 (right). Bottom panels: time series of spatially averaged July mean bottom temperatures, relative to the 2015–2044 average of each statistically downscaled model under SSP126 (left) and SSP585 (right). Thick lines indicate ensemble average for each SSP.

subtle shifts in the phenology or high-frequency statistics of the global model output (e.g. more frequent storms, leading to greater mixing). Here, as with H19, we chose to use the uncorrected global forcing, and instead focus on the changes in the regional response over time (itself an alternate "delta" method).

It could be argued that our use of monthly time series, taken together year by year, artificially limits our focus to covariance within a single calendar year, hence excluding covariance of, say, bottom temperature in fall from bottom temperature in the subsequent spring. We explored this possibility using a collection of 24 months instead of 12, and found no substantial difference in the monthly patterns.

It could further be argued that stronger correlations between forcing and response can be found using single variable pairs, e.g. air temperature and bottom temperature, and subsequently used for regional projections. This is certainly true, but could potentially result in dynamically inconsistent projections of the system, such as temperature and salinity fields out of balance with velocities. In addition, the covariant patterns account for significant co-linearity of forcing terms (air temperature, absolute humidity) and more clearly suggest mechanisms which entail multiple variables lagged in time (air temperature, ice, salinity, plankton). Indeed, the mechanisms suggested could be fruitfully explored by expanding our analysis to include heat and biomass flux variables from the regional model.

In this study we derived the multivariate modes using a concatenated series of monthly anomalies derived separately from each downscaling realization. A related approach would be to derive multiviate modes separately for each realization (or each ESM), followed by averaging across realizations. We have not yet tested this alternative, which could more fully identify unique modes of covariability from different forcings. However, it is noteworthy that at least one of our modes (the second) was primarily associated with a particular ESM, and that our chosen method was able to extract that association out of the full, concatenated series.

Alternate possible methods to achieve a compact summary of regional model behavior include a modified use of Linear Inverse Modeling, which has been used for seasonal predictions (e.g. Newman et al., 2003; Alexander et al., 2008; Capatondi and Sardeshmukh, 2015), and the use of Machine Learning to relate the forcing to the response, trained on the existing set of dynamically downscaled output. These both typically entail dimensional reduction of the type used here, that is, univariate EOF decomposition as a first step. We are presently exploring these alternate methods. The appeal of pure EOF decomposition - including the variant used in this study - lies in its ability to reconstruct the entire dataset using a set of fully orthogonal modes. In some circumstances this requirement for orthogonality is considered a liability, especially as the modes, derived from mathematical decomposition, can lack any "true" physical meaning (Dommenget and Latif, 2002). Their virtue lies in their ability to summarize covariance among a large collection of properties, as opposed to looking at one-by-one correlations among all pairs of samples. In our ecosystems context, this helps to ferret out emergent properties involving many state variables. Machine Learning methods may ultimately do better at relating multivariate, spatially distributed series to one another (e.g. predicting one set of series from a different set), but may be harder to interpret mechanistically.

4.4. *Known issues of the models*

While the present regional model corrects several deficiencies of the previous version, some known issues remain. 1) A known feature of the present code (and the H16 version) is an exaggerated acceleration of primary production with temperature; it is not presently known how large of an impact this has on the results. 2) The boundary conditions presently used for plankton (radiation plus nudging to seed values), while presumed adequate for phytoplankton (given their rapid turnover), may distort zooplankton fields near the boundaries, as they take longer to come into balance with the ambient nutrients. More generally, it is challenging to map plankton functional groups from the global ESMs

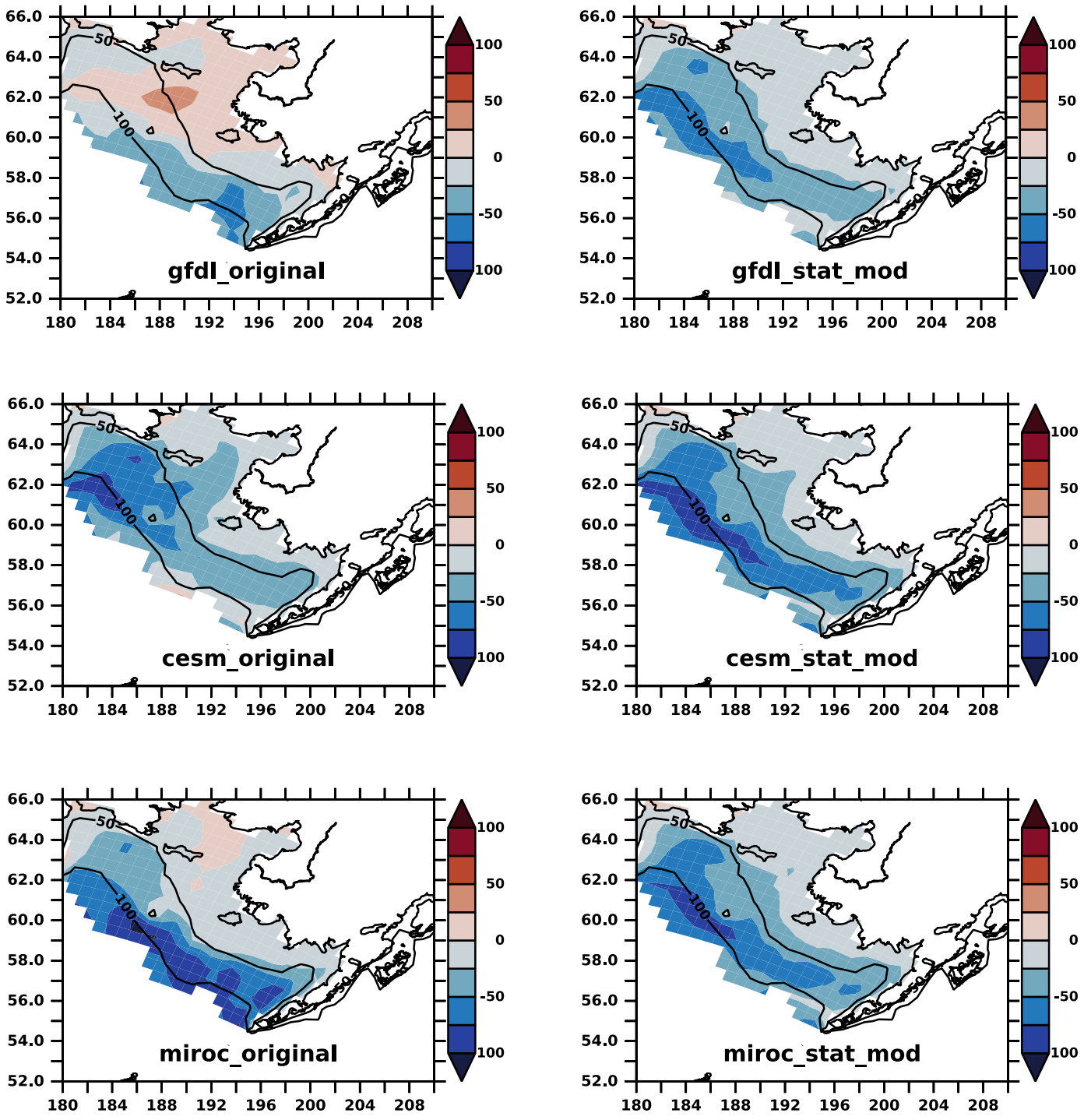

Fig. 21. As in Fig. 19, for July depth-integrated shelf Euphausiids (EupS, mg C m^{-2}).

onto their regional equivalent - as different categories are used in each model.

The CMIP6 ESMs used for this study had significant improvements over CMIP5, described in C21 and Eyring et al. (2016). Nonetheless, certain deviations from observed present-day aspects of the Bering Sea were observed in the historical CMIP6 output. In particular, the MIROC model exhibited substantial offshore winds and corresponding offshore surface flows during much of the year in both historical and projection runs; these were unrealistically large and persistent relative to observed climatology. This underscores the need to focus on changes in projected results over the 21st century in these simulations, rather than absolute values. Stated another way: to the extent that averaged dynamics are quasi-linear, projected *changes* are less biased than the specific variable *values* at some present or future date. This is of course less true when many processes are very nonlinear; in that case, if values are biased, changes to those values are more likely to be biased as well.

5. Conclusions

Based on air temperatures from a broad 40-member ensemble of global models, the anticipated coupled biophysical change in the Bering Sea is approximately 4x greater under SSP585 than under SSP126; for example, a mean covariant rise in July bottom temperatures of 4 degrees C under SSP585, as compared to 1 degree C under SSP126, and a mean

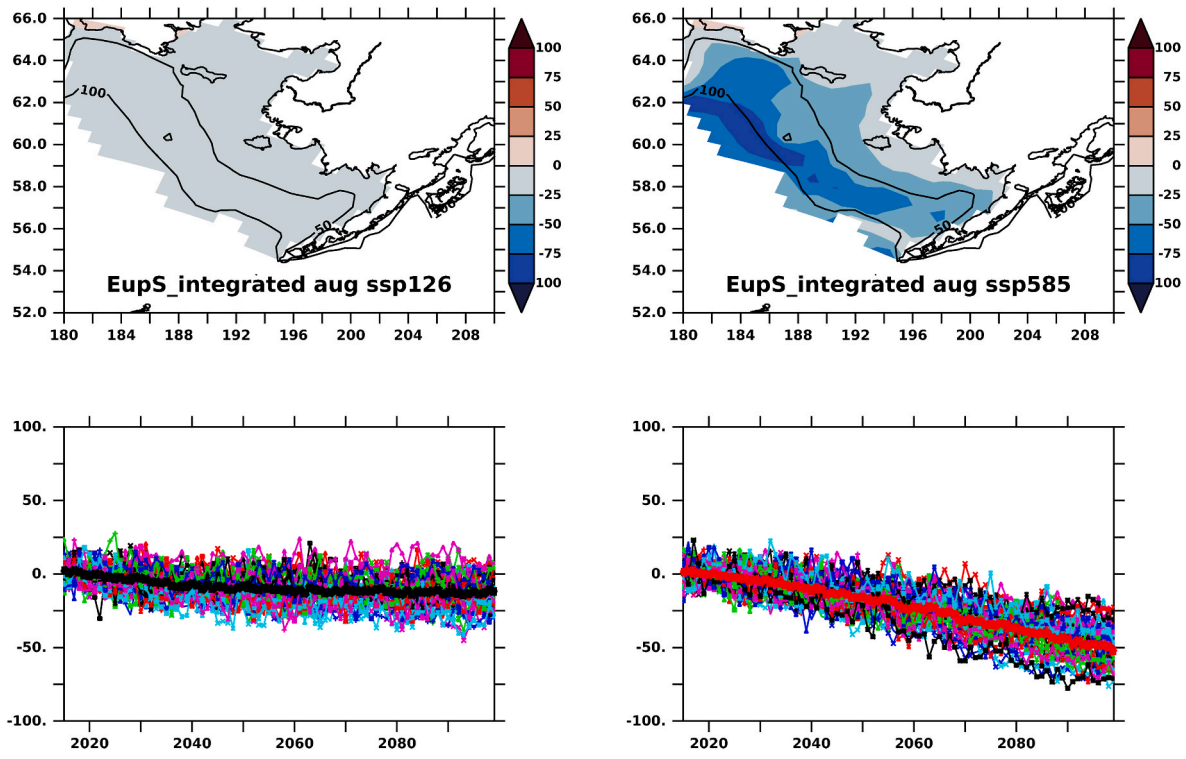

Fig. 22. As in Fig. 20, for July depth-integrated shelf Euphausiids (EupS, mg C m^{-2}).

covariant decrease in July depth-integrated shelf Euphausiids of ~50 gC m^{-2} under SSP585, as compared to ~12 gC m^{-2} under SSP126. These two features both stabilize at new equilibria after 2060 under SSP126, whereas this does not occur by 2100 under SSP585. This multivariate analysis of dynamically downscaled results for the Bering Sea indicates that, at a systems level, rising air and ocean temperatures from the global models are strongly coupled with rising regional temperatures and reduced ice cover/thickness in the Bering Sea, as well as strong changes to the phenology of its plankton food chain (earlier blooms), and reduced biomass of large zooplankton in the late summer through fall. These findings support interpretations based on individual variables, but emphasize how particular components of the system co-vary through time on interannual through interdecadal time scales. The hybrid dynamical-statistical method used here provides a compact way to estimate the changes to many regional attributes under a variety of global change scenarios, and hence may be useful for future studies exploring the implications of projected changes on Bering Sea ecological and social systems under those scenarios.

Authorship statement

Albert J. Hermann: Conceptualization, Data curation, Formal analysis, Methodology, Software, Validation, Visualization, Writing - original draft, Writing - review & editing. **Kelly Kearney:** Conceptualization, Data curation, Methodology, Software, Visualization, Writing - original draft, Writing - review & editing. **Wei Cheng:** Conceptualization, Data curation, Methodology, Software, Visualization, Writing - original draft, Writing - review & editing. **Darren Pilcher:** Conceptualization, Methodology, Software. **Kerim Aydin:** Conceptualization. **Kirstin K. Holsman:** Conceptualization, Funding acquisition, Project administration, Writing - original draft. **Anne B. Hollowed:** Conceptualization, Funding acquisition, Project administration.

Declaration of competing interest

The authors declare that they have no known competing financial interests or personal relationships that could have appeared to influence the work reported in this paper.

Acknowledgements

This work was facilitated through the use of advanced computational, storage, and networking infrastructure provided by the Hyak supercomputer system at the University of Washington. Funding for this project was provided by NOAA OAR (RTAP) and NOAA NMFS (FATE and IEA). We thank Dr. Edward D. Cokelet and two anonymous reviewers for constructive comments on an earlier version of the manuscript. We acknowledge the World Climate Research Programme, which, through its Working Group on Coupled Modelling, coordinated and promoted CMIP6. We thank the climate modeling groups for producing and making available their model output, the Earth System Grid Federation (ESGF) for archiving the data and providing access, and the multiple funding agencies who support CMIP6 and ESGF. We thank Jasmin John, Aparna Radhakrishnan and Hans Vahlenkamp for their assistance with GFDL data. This work is partially funded by University of Washington/Cooperative Institute for Climate, Ocean, and Ecosystem Studies (CICOES) under NOAA Cooperative Agreement NA15OAR4320063. This is CICOES contribution 2021-1164, PMEL contribution 5241, and EcoFOCI–1012.

Appendix A. Supplementary data

Supplementary data to this article can be found online at https://doi.org/10.1016/j.dsr2.2021.104974.

References

Alexander, M.A., Matrosova, L., Penland, C., Scott, J.D., Chang, P., 2008. Forecasting Pacific SSTs: linear inverse model predictions of the PDO. J. Clim. 21 (2), 385–402.
Budgell, W.P., 2005. Numerical simulation of ice-ocean variability in the Barents Sea region: towards dynamical downscaling. Ocean Dynam. 55, 370–387.
Bretherton, C.S., Smith, C., Wallace, J.M., 1992. An intercomparison of methods for finding coupled patterns in climate data. J. Clim. 5, 541–560.

Capotondi, A., Sardeshmukh, P.D., 2015. Optimal precursors of different types of ENSO events. Geophys. Res. Lett. 42, 9952–9960. https://doi.org/10.1002/2015GL066171.

Cheng, W., Curchitser, E., Ladd, C., Stabeno, P.J., Wang, M., 2014. Influences of sea ice on the eastern Bering Sea: NCAR CESM simulations and comparison with observations. Deep-Sea Res. II 109, 27–38. https://doi.org/10.1016/j.dsr2.2014.03.002.

Cheng, Wei, Hermann, Albert, Hollowed, Anne, Holsman, Kirstin, Kelly, Kearney, Pilcher, Darren, Stock, Charles, Aydin, Kerim, 2021. Bering Sea Dynamical Downscaling: Environmental and Lower Trophic Level Responses to Climate Forcing in CMIP6. Deep-Sea Research II. In this issue. https://doi.org/10.1016/j.dsr2.2021.104975.

Coachman, L.K., 1986. Circulation, water masses, and fluxes on the southeastern Bering Sea shelf. Continent. Shelf Res. 5 (1–2), 23–108.

Cokelet, E.D., 2016. 3-D water properties and geostrophic circulation on the eastern Bering Sea shelf. Deep Sea Res. Part II Top. Stud. Oceanogr. 134, 65–85.

Coyle, K.O., Eisner, L.B., Mueter, F.J., Pinchuk, A.I., Janout, M.A., Cieciel, K.D., Farley, E.V., Andrews, A.G., 2011. Climate change in the southeastern Bering Sea: impacts on pollock stocks and implications for the Oscillating Control Hypothesis. Fish. Oceanogr. 20 (2), 139–156.

Danabasoglu, G., Lamarque, J.-F., Bacmeister, J., Bailey, D.A., DuVivier, A.K., Edwards, J., et al., 2020. The community earth system model version 2 (CESM2). J. Adv. Model. Earth Syst. 12 (2), e2019MS001916 https://doi.org/10.1029/2019MS001916.

Danielson, S., Curchitser, E., Hedstrom, K., Weingartner, T., Stabeno, P., 2011. On ocean and sea ice modes of variability in the Bering Sea. J. Geophys. Res. 116, C12034 https://doi.org/10.1029/2011JC007389.

Dommenget, D., Latif, M., 2002. A cautionary note on the interpretation of EOFs. J. Clim. 15 (2), 216–225.

Drenkard, E., co-authors, 2021. Next-generation regional ocean projections for living marine resource management in a changing climate. ICES (Int. Counc. Explor. Sea) J. Mar. Sci. 78 (6), 1969–1987. https://doi.org/10.1093/icesjms/fsab100.

Duffy-Anderson, J.T., Stabeno, P.J., Siddon, E.C., Andrews, A.G., Cooper, D.W., Eisner, L.B., Farley, E.V., Harpold, C.E., Heintz, R.A., Kimmel, D.G., Sewall, F.F., Spear, A.H., Yasumishii, E.C., 2017. Return of warm conditions in the southeastern Bering sea: phytoplankton - fish. PLoS One 12 (6), e0178955. https://doi.org/10.1371/journal.pone.0178955.

Dunne, J.P., Horowitz, L.W., Adcroft, A.J., Ginoux, P., Held, I.M., John, J.G., et al., 2020. The GFDL earth system model version 4.1 (GFDL-ESM 4.1): overall coupled model description and simulation characteristics. J. Adv. Model. Earth Syst. 12 (11), e2019MS002015 https://doi.org/10.1029/2019MS002015.

Eyring, V., Bony, S., Meehl, G.A., Senior, C.A., Stevens, B., Stouffer, R.J., Taylor, K.E., 2016. Overview of the coupled model intercomparison project phase 6 (CMIP6) experimental design and organization. Geosci. Model Dev. (GMD) 9, 1937–1958. https://doi.org/10.5194/gmd-9-1937-2016.

Fissel, B., Dalton, M., Garber-Yonts, B., Haynie, A., Kasperski, S., Lee, J., Sparks, K., 2017. Stock assessment and fishery evaluation report for the groundfish fisheries of the Gulf of Alaska and Bering Sea/Aleutian Islands area: economic status of the groundfish fisheries of Alaska, 2016. NPFMC Bering Sea, Aleutian Islands and Gulf of Alaska SAFE. Seattle, WA. Retrieved from. http://www.afsc.noaa.gov/refm/docs/2017/economic.pdf.

Gibson, G.A., Spitz, Y.H., 2011. Impacts of biological parameterisation, initial conditions, and environmental forcing on parameter sensitivity and uncertainty in a marine ecosystem model for the Bering Sea. J. Mar. Syst. 88, 214–231.

Haidvogel, D.B., Arango, H., Budgell, W.P., Cornuelle, B.D., Curchitser, E., Di Lorenzo, E., Fennel, K., Geyer, W.R., Hermann, A.J., Lanerolle, L., Levin, J., McWilliams, J.C., Miller, A.J., Moore, A.M., Powell, T.M., Shchepetkin, A.F., Sherwood, C.R., Signell, R.P., Warner, J.C., Wilkin, J., 2008. Regional Ocean forecasting in terrain-following coordinates: model formulation and skill assessment. J. Comput. Phys. 227, 3595–3624.

Hajima, T., Watanabe, M., Yamamoto, A., Tatebe, H., Noguchi, M.A., Abe, M., Ohgaito, R., Ito, A., Yamazaki, D., Okajima, H., Ito, A., Takata, K., Ogochi, K., Watanabe, S., Kawamiya, M., 2020. Development of the MIROC-ES2L Earth system model and the evaluation of biogeochemical processes and feedbacks. Geosci. Model Dev. (GMD) 13, 2197–2244. https://doi.org/10.5194/gmd-13-2197-2020.

Haynie, A.C., Huntington, H.P., 2016. Strong connections, loose coupling: the influence of the Bering Sea ecosystem on commercial fisheries and subsistence harvests in Alaska. Ecol. Soc. 21 (4) https://doi.org/10.5751/ES-08729-210406 art6.

Hermann, A.J., Gibson, G.A., Bond, N.A., Curchitser, E.N., Hedstrom, K., Cheng, W., Wang, M., Stabeno, P.J., Eisner, L., Cieciel, K.D., 2013. A multivariate analysis of observed and modeled biophysical variability on the Bering Sea shelf: multidecadal hindcasts (1970-2009) and forecasts (2010-2040). Deep Sea Res. II 94, 121–139. https://doi.org/10.1016/j.dsr2.2013.04.007.

Hermann, A.J., Gibson, G.A., Bond, N.A., Curchitser, E.N., Hedstrom, K., Cheng, W., Wang, M., Cokelet, E.D., Stabeno, P.J., Aydin, K., 2016a. Projected future biophysical states of the Bering Sea. Deep-Sea Res. II 134, 30–47. https://doi.org/10.1016/j.dsr2.2015.11.001.

Hermann, A.J., Ladd, C., Cheng, W., Curchitser, E.N., Hedstrom, K., 2016b. A model-based examination of multivariate physical modes in the eastern and western Gulf of Alaska. Deep-Sea Res. II. https://doi.org/10.1016/j.dsr2.2016.04.005i.

Hermann, A.J., Gibson, G.A., Cheng, W., Ortiz, I., Aydin, K., Wang, M., Hollowed, A.B., Holsman, K.K., 2019. Projected biophysical conditions of the Bering Sea to 2100 under multiple emission scenarios. ICES J. Mar. Sci. 76 (5), 1280–1304. https://doi.org/10.1093/icesjms/fsz043.

Holsman, K.K., Haynie, A.C., Hollowed, A.B., Reum, J.C.P., Aydin, K., Hermann, A.J., et al., 2020. Ecosystem-based fisheries management forestalls climate-driven collapse. Nat. Commun. 11 (1) https://doi.org/10.1038/s41467-020-18300-3.

Holsman, K., Hollowed, A., Ito, S., Bograd, S., Hazen, E., King, J., Perry, R.I., 2018. Climate change impacts, vulnerabilities and adaptations: north Pacific and Pacific Arctic marine fisheries. In: Barange, M., Bahri, T., Beveridge, M.C.M., Cochrane, K. L., Funge-Smith, S., Poulain, F. (Eds.), Impacts of Climate Change on Fisheries and Aquaculture: Synthesis of Current Knowledge, Adaptation and Mitigation Options, vol. 627, pp. 113–138 (Rome: FAO Fisheries and Aquaculture Technical Paper).

Hollowed, A.B., Holsman, K.K., Haynie, A.C., Hermann, A.J., Punt, A.E., Aydin, K.Y., et al., 2020. Integrated modeling to evaluate climate change impacts on coupled social-ecological systems in Alaska. Front. Mar. Sci. 6 (January), 1–18. https://doi.org/10.3389/fmars.2019.00775.

Hunt Jr., G, L., Stabeno, P., Walters, G., Sinclair, E., Brodeur, R.D., Napp, J.M., Bond, N. A., 2002. Climate change and control of the southeastern Bering Sea pelagic ecosystem. Deep-Sea Res. Pt. II 49 (26), 5821–5853. https://doi.org/10.1016/S0967-0645(02)00321-1.

Hunt Jr., G, L., Coyle, K.O., Eisner, L., Farley, E.V., Heintz, R., Mueter, F., Napp, J.M., Overland, J.E., Ressler, P.H., Salo, S., Stabeno, P.J., 2011. Climate impacts on eastern Bering Sea foodwebs: a synthesis of new data and an assessment of the Oscillating Control Hypothesis. ICES J. Mar. Sci. 68 (6), 1230–1243. https://doi.org/10.1093/icesjms/fsr036.

IPCC, 2013. Climate change 2013: the physical science basis. In: Stocker, T.F., Qin, D., Plattner, G.K., Tignor, M.M.B., Allen, S.K., Boschung, J., et al. (Eds.), Contribution of Working Group I to the Fifth Assessment Report of the Intergovern Mental Panel on Climate Change. Cambridge University Press, Cambridge, United Kingdom and New York, NY, USA, p. 1535. https://doi.org/10.1017/CBO9781107415324.Summary.

IPCC, 2014. In: Barros, V.R., Field, C.B., Dokken, D.J., Mastrandrea, M.D., Mach, K.J., Bilir, T.E., et al. (Eds.), Climate Change 2014: Impacts, Adaptation, and Vulnerability Part. B: Regional Aspects. Cambridge University Press, Cambridge, UK and New York, New York, USA. https://doi.org/10.1007/s13398-014-0173-7.2.

Jones, M.C., Berkelhammer, M., Keller, K.J., Yoshimura, K., Wooller, M.J., 2020. High sensitivity of Bering Sea winter sea ice to winter insolation and carbon dioxide over the last 5500 years. Sci. Adv. 6 (36), eaaz9588.

Kachel, N.B., Hunt Jr., G, L., Salo, S.A., Schumacher, J.D., Stabeno, P.J., Whitledge, T.E., 2002. Characteristics and variability of the inner front of the southeastern Bering Sea. Deep-Sea Res. Pt. II 49 (26), 5889–5909. https://doi.org/10.1016/S0967-0645(02)00324-7.

Kearney, K.A., 2019. Freshwater input to the Bering sea, 1950–2017. U.S. Dep. Commer. NMFS-AFSC-388 NOAA Tech. Memo. 46 (Document).

Kearney, K., Hermann, A., Cheng, W., Ortiz, I., Aydin, K., 2020. A coupled pelagic–benthic–sympagic biogeochemical model for the Bering Sea: documentation and validation of the BESTNPZ model (v2019.08.23) within a high-resolution regional ocean model. Geosci. Model Dev. (GMD) 13, 597–650. https://doi.org/10.5194/gmd-13-597-2020.

Kinder, T.H., Schumacher, J.D., 1981. Hydrographic structure over the continental shelf of the southeastern Bering Sea. In: Hood, D.W., Calder, J.A. (Eds.), Chapter 4 in *Eastern Bering Sea Shelf: Oceanography And Resources*, vol. 1. USDOC/NOAA/OMPA, 31–51.

Large, W.G., Yeager, S.G., 2008. The global climatology of an interannually varying air-sea 1009 flux data set. Clim. Dynam. 33, 341–364.

Large, W.G., McWilliams, J.C., Doney, S.C., 1994. Oceanic vertical mixing: a review and a model with a nonlocal boundary layer parameterization. Rev. Geophys. 32, 363–403.

Li, L., McClean, J., Miller, A., Eisenman, I., Hendershott, M., Papadopoulos, C., 2014a. Processes driving sea ice variability in the Bering Sea in an eddying ocean/sea ice model: mean seasonal cycle. Ocean Model. 84, 51–66. https://doi.org/10.1016/j.ocemod.2014.09.006.

Li, L., Miller, A., McClean, J., Eisenman, I., Hendershott, M., 2014b. Processes driving sea ice variability in the Bering Sea in an eddying ocean/sea ice model: anomalies from the mean seasonal cycle. Ocean Dynam. 64, 1693–1717. https://doi.org/10.1007/s10236-014-0769-7.

Meehl, G.A., Covey, C., Delworth, T., Latif, M., McAvaney, B., Mitchell, J.F.B., Stouffer, R.J., Taylor, K.E., 2007. The WCRP CMIP3 multimodel dataset: a new era in climate change research. Bull. Am. Meteorol. Soc. 88, 1383–1394.

Marchesiello, P., McWilliams, J.C., Shchepetkin, A., 2001. Open boundary conditions for long-term integration of regional oceanic models. Ocean Model. 3, 1–20.

Newman, M., Sardeshmukh, P.D., Winkler, C.R., Whitaker, J.S., 2003. A study of subseasonal predictability. Mon. Weather Rev. 131 (8), 1715.

O'Neill, B.C., Tebaldi, C., van Vuuren, D.P., Eyring, V., Friedlingstein, P., Hurtt, G., et al., 2016. The scenario model intercomparison project (ScenarioMIP) for CMIP6. Geosci. Model Dev. (GMD) 9 (9), 3461–3482. https://doi.org/10.5194/gmd-9-3461-2016.

Ortiz, I., Aydin, K., Hermann, A.J., Gibson, G., Punt, A.E., Wiese, F., Eisner, L.B., Ferm, N., Buckley, T.W., Moffitt, E.A., Ianelli, J.N., Murphy, J., Dalton, M., Cheng, W., Wang, M., Hedstrom, K., Curchitser, E.N., Bond, N.A., Boyd, C., 2016. Climate to fish: synthesizing field work, data and models in a 39-year retrospective analysis of seasonal processes on the eastern Bering Sea shelf and slope. Deep-Sea Res. II. https://doi.org/10.1016/j.dsr2.2016.07.009.

Pilcher, D.J., Cross, J.N., Hermann, A., Kearney, K., Cheng, W., Mathis, J.T., 2021. Dynamically Downscaled Projections of Ocean Acidification for the Bering Sea. Deep-Sea Research II (this volume, in review).

Preisendorfer, R.W., 1988. Principal Component Analysis in Meteorology and Oceanography. Elsevier, Amsterdam.

Punt, A.E., Butterworth, D.S., de Moor, C.L., De Oliveira, J.A.A., Haddon, M., 2016. Management strategy evaluation: best practices. Fish Fish. 17, 303–334. https://doi.org/10.1111/faf.12104.

Reum, Jonathan, Blanchard, Julia, Holsman, Kirstin, Aydin, Kerim, Babcock Hollowed, Anne, Hermann, Albert J., Cheng, Wei, Faig, Amanda, Haynie, Alan C., Andre, Punt, 2020. Ensemble projections of future climate change impacts on the Eastern Bering Sea food web using a multispecies size spectrum model. Front. Mar. Sci. Sec. Global Change Future Ocean 7, 124.

Shchepetkin, A.F., McWilliams, J.C., 2005. The regional oceanic modeling system (ROMS): a split-explicit, free-surface, topography-following-coordinate oceanic model. Ocean Model. 9 (4), 347–404.

Sigler, M.F., Napp, J.M., Stabeno, P.J., Heintz, R.A., Lomas, M.W., Hunt, G.L., 2016. Variation in annual production of copepods, euphausiids, and juvenile walleye pollock in the southeastern Bering Sea. Deep Sea Res. Part II Top. Stud. Oceanogr. 134, 223–234. https://doi.org/10.1016/j.dsr2.2016.01.003.

Stabeno, P.J., Napp, J., Mordy, C., Whitledge, T., 2010. Factors influencing physical structure and lower trophic levels of the eastern Bering Sea shelf in 2005: sea ice, tides and winds. Prog. Oceanogr. 85 (3–4), 180–196. https://doi.org/10.1016/j.pocean.2010.02.010.

Stabeno, P.J., Kachel, N.B., Moore, S.E., Napp, J.M., Sigler, M., Yamaguchi, A., Zerbini, A.N., 2012. Comparison of warm and cold years on the southeastern Bering Sea shelf and some implications for the ecosystem. Deep-Sea Res. II 65–70, 14–30. https://doi.org/10.1016/j.dsr2.2012.02.019.

Stabeno, P.J., Danielson, S., Kachel, D., Kachel, N.B., Mordy, C.W., 2016. Currents and transport on the eastern Bering Sea shelf: an integration of over 20 years of data. Deep-Sea Res. II 134, 13–29. https://doi.org/10.1016/j.dsr2.2016.05.010 (Understanding Ecosystem Processes in the Eastern Bering Sea IV).

Stabeno, P.J., Duffy-Anderson, J.T., Eisner, L.B., Farley, E.V., Heintz, R.A., Mordy, C.W., 2017. Return of warm conditions in the southeastern Bering Sea: physics to fluorescence. PLoS One 12 (9), e0185464. https://doi.org/10.1371/journal.pone.0185464 (Open access).

Stabeno, Phyllis J., Bell, S.W., 2019. Extreme conditions in the Bering sea (2017–2018): record-breaking low sea-ice extent. Geophys. Res. Lett. January 1979, 2019GL083816 https://doi.org/10.1029/2019GL083816.

Sullivan, M.E., Kachel, N.B., Mordy, C.W., Salo, S.A., Stabeno, P.J., 2014. Sea ice and water column structure on the eastern Bering sea shelf. Deep-Sea Res. II 109, 39–56. https://doi.org/10.1016/j.dsr2.2014.05.009.

Taylor, K.E., Stouffer, R.J., Meehl, G.A., 2012. An overview of CMIP5 and the experiment design. Bull. Am. Meteorol. Soc. 93, 485–498.

Thorson, James T., Wei Cheng, Al Hermann, Ianelli, James N., Litzow, Michael A., O'Leary, Cecilia, Thompson, Grant, 2020. Empirical Orthogonal Function Regression: linking population biology to spatial varying environmental conditions in end-of-century forecasts. Global Change Biol. 26 (8), 4638–4649.